"COMPUTATIONAL STUDIES OF PHYSICAL PROPERTIES OF BORON CARBIDE"

FINAL SCIENTIFIC/TECHNICAL REPORT

Reporting Period January 1, 2009 through Jun 30, 2011

Lizhi Ouyang

July 30, 2012

DOE Award Number: DE-FE0000103

Principle Investigator: Lizhi Ouyang
Tennessee State University
3500 John A. Merritt Blvd.
Nashville, Tennessee 37209

Subcontractor: Wai-Yim Ching
University of Missouri-Kansas City
5100 Rockhill Road
Kansas City, MO 64110

DISCLAMER

This report was prepared as an account of work sponsored by an agency of the United States Government. Neither the Unite States Government nor any agency thereof, no any of the employees, makes any warranty, express or implied, or assumes any legal liability or responsibility for accuracy, completeness, or usefulness of any information, apparatus, product, or process disclosed, or represents that its use would not infringe privately owned rights. Reference herein to any specific commercial product, process, or service by trade name, trademark, manufacturer, or otherwise does not necessarily constitute or imply its endorsement, recommendation, or favoring by the United States Government or any agency thereof. The views or opinions or authors expressed herein do not necessarily state or reflect those of the United States Government or any agency thereof.

ABSTRACT

The overall goal is to provide valuable insight in to the mechanisms and processes that could lead to better engineering the widely used boron carbide which could play an important role in current plight towards greener energy. Carbon distribution in boron carbide, which has been difficult to retrieve from experimental methods, is critical to our understanding of its structure-properties relation. For modeling disorders in boron carbide, we implemented a first principles method based on supercell approach within our G(P,T) package. The supercell approach was applied to boron carbide to determine its carbon distribution. Our results reveal that carbon prefers to occupy the end sites of the 3-atom chain in boron carbide and further carbon atoms will distribute mainly on the equatorial sites with a small percentage on the 3-atom chains and the apex sites. Supercell approach was also applied to study mechanical properties of boron carbide under uniaxial load. We found that uniaxial load can lead to amorphization. Other physical properties of boron carbide were calculated using the G(P,T) package.

Table of Contents

I. EXECUTIVE SUMMARY

This report summarizes our method development, software implementation, infrastructure improvement and computational studies for the boron carbide system during the two and half year period over which we have developed supercell approaches for modeling disorders and applied them to investigate structure-properties relation in boron carbide.

Structure of boron carbide is often described to have a 15-atom primitive cell with R-3m space group symmetry. Its atomic structure however is very complex as the carbon atoms randomly distribute on all 15 lattice sites. Furthermore, in practice, boron carbide is always carbon deficient.

To study disordered system like boron carbide, we have developed three methods which are implemented as modules in our G(P,T) package:

- **Supercell method**. The large supercell models provide configuration freedom for calculating the carbon distribution.
- **Unitcell expansion method**. Rigorous approach such as cluster expansion method is computationally prohibitive for boron carbide as partial occupations can be found on all 15 lattice sites. To overcome the challenge of complex lattices, we developed a coarse-grained unitcell expansion method in which each unitcell is considered a site thus greatly reduces the lattice complexity at the expense of more types at each site.

Additional modules for physical properties calculations are also developed:

- **Pressure dependent elastic constants**.
- **Structure modeler that generate supercells, surface slabs and interfaces**.
- Input generator for first principles calculations based on our internal structure format.
- Job manager for automating and parallelizing the complex physical properties calculations that involves many different kinds of input setups for those first principles calculations.

Carbon distribution in boron carbide is central to understand its structure-properties relation. Determination of carbon distribution from experiments has so far been inconclusive due to various technical issues. We used both the supercell method and the unitcell expansion method to study the carbon distribution. Our results suggest that depending on the carbon concentration, starting from lower end:

- The carbon first filled the end sites of the 3-atom chains in boron,
- Additional carbon will take the equatorial sites in the B_{12} icosahedrons with a small percentage will go to the central site of the 3-atom chains.
- At higher carbon concentration, $[B_{10}C_2]$C-B-C type of structure started to emerge.

We further studied the mechanical behavior of boron carbide under uniaxial load. Boron carbide suffers from dramatic decrease of shear strength when impact goes beyond the Hugonoit Elastic Limit (HEL) of about 22GPa. Post-failure analysis attributes the loss of shear strength to local amorphization. We performed uniaxial compression simulation of boron carbide using a supercell model. We observed, however, amorphization of boron carbide at much higher stress of about 160GPa.

For selected models, we computed the vibrational properties and X-ray absorption near edge structure. We also searched extensively high symmetry supercell models and did not find any low energy configuration that warrants further studies.

To facilitate our software development, we had built an 18-node computer cluster (gpt.tsuniv.edu) with off-the-shell components with total budget less than $10K.

II. INTRODUCTION

Background

Boron carbide is a class of material with composition stiochiometry in the form of $B_{12-x}C_{3-x}$ ($0.06<x<1.7$)[**1**]. It has great application in energy application owing to its many unusual properties such as light weight, high mechanic strength, high melting temperature, high chemical inertness, and high efficiency direct thermoelectric conversion *etc* [**2, 3, 4, 5**].

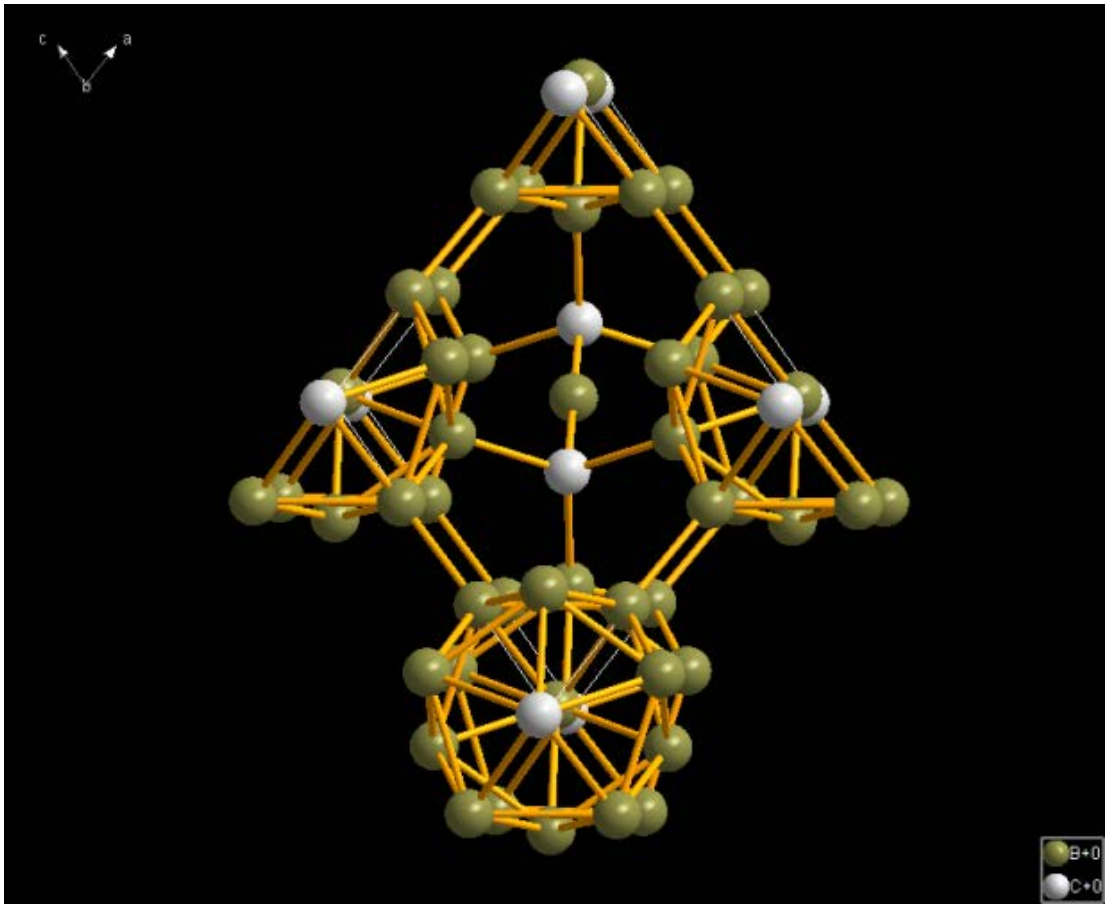

Figure 1. Ball-stick model of a 15 atom crystal model of B4C. Gray and white represent B and C, respectively

Depending on preparation condition, boron carbide can be amorphous, polycrystal ceramics or a large single crystal. Crystal boron carbide has a lattice structure of space group R-3m, as depicted in figure 1,

consisting of a twelve atom icosahedron and a 3-atom chain. The lattice structure of boron carbide can be understood as a closely package isocahedron with part of the interstitial regions filled with 3-atom chains. While the location of lattice sites has been resolved a long time ago, distribution of the carbon atoms, however, remains controversial [**6, 7, 8**]. The lack of conclusive experimental evidences to locate the carbon atoms in the crystal lattice is largely due to similar cross section of boron and carbon atoms in X-ray or neutron scattering. Previous work trying to use vibrational, electronic, or nuclear finger prints to pin down the locations of the carbon atoms has so far met only limited successes [**9, 10, 11, 12, 13**]. Theoretical investigations had also been carried out for some specific stoichiometric models or small crystal models[**14, 15, 9, 13**]. These experimental and theoretical findings indicate carbon may exist as substitutional disorder at the icosahedrons sites and the atom chains or as interstitial defect between the icosahedrons. Below 8%, boron carbide becomes mixed phases as pure boron starts to precipitate. X-ray studies[**16**] supported by some DFT calculations[**17, 18**] suggest that the decreasing of carbon content is accompanied by gradual replacement of carbon by boron in the icosahedrons, while neutron diffraction[**19**], IR/Raman spectra[**20**], and some other studies[**21, 22, 23, 6**] indicate that the preferential replacement sites are located on the atom chains. Recently, Hoffman[**24**] *etc* attempted to resolve the mysteries of boron carbide by tracking the molecular orbital evolution from fragments to lattice and concluded that the mysteries of boron carbide might be due to carbon substitution disorder.

In previous theoretical studies, the structural models used for boron carbide are limited in the size which may not be as adequate to describe the carbon distribution in boron carbide containing substitutional disordered, defective, or both. The small size also means the vibrational, electronic finger print used as evidences for certain local structures may not be as reliable as atomic interaction sphere is at the same level of cell size. Therefore, it is highly desirable to study boron carbide using large supercell models.

Supercell Approach for Disordered System

We used a supercell approach to study the structure-properties relation of the disordered boron carbide with various carbon concentrations. The advantages of using supercells for modeling disordered boron carbide include: (1) methods developed for periodic system can be readily applied; (2) providing larger configuration space for better description of disorder, for example, it is possible to use method such as cluster expansion approach[**25**] to estimate the configuration entropy contribution to free energy which can be crucial to the stability of disordered lattice; (3) straightforward for supercell based X-ray absorption near edge structure (XANES) or energy loss near edge structure (ELNES) calculation and phonon calculation. The disadvantages may include high computational cost and the lack of standard to determine the sufficient supercell size.

We implemented the supercell approach in three steps. First, supercell models were generated using several approaches implemented in our G(P,T) package. Next, the resulting supercell models were analyzed for their symmetries using method described in previous work on zirconium silicate and alumina oxide where novel new phases had been identified[**26, 27, 28**]. Total energies of these models were subsequently calculated using first principles method. Those lower energy models were marked for further analysis. At last, selected supercell models of lowest total energies were optimized. Further analysis for its physical properties including electronic and vibrational structure and finger prints, mechanical and thermodynamic properties were performed if deemed necessary.

III. Methods and Software Developments

Prior Work

Lattice dynamics with the G (P, T) package

We had developed the G(P,T) package capable of computing elastic tensor, phonon structure, Helmoltz and Gibbs free energy and many other thermodynamic properties such as entropy, heat capacity,

isothermal bulk modulus, thermal expansion coefficient, and Grüneisen parameters, etc. The G(P,T) package were parallelized at task level and successfully tested on supercomputers of NERSC.

G(P,T) package was implemented as an easy-deploy script based job management and automation system. It included an elastic properties module, a phonon calculation module, a Born effective charge module, an optical and dielectric properties module, a job management and automation module, and a box of analysis and graphic tools for phonon, thermodynamic properties, elastic waves, and dielectric properties *etc*. G(P,T) calculates the free energy of solid with Born-Oppenheimer approximation that separates electron and ion motion. Electronic contribution to free energy is calculated using first principles method such as VASP [**29, 30, 31**]. Ionic contribution to free energy is calculated using semi-classical lattice dynamic approach. Volume dependent lattice free energies were calculated using quasi-harmonic approximation in which the lattices were considered harmonic at each volume and free energies of harmonic lattices can be calculated from their force constant matrices. G(P,T) package computes the force constant matrix using finite difference approach with energy and force evaluated by a first principles method. Phonon structure is then obtained from the dynamic matrix constructed based on force constant matrix. Once phonon spectrum is obtained, it is possible to estimate all other thermodynamic functions. The free energy *F(V,T)* at temperature *T* and volume *V* is given by,

$$
\begin{aligned}
&F(V,T) = F^{elec}(V,T) + F^{vib}(V,T) = U^{elec}(V,0) + F^{elec,T}(V,T) + F^{vib}(V,T) \\
&F^{elec,T}(V,T) \approx -\sum_i k_B T \ln(1 + e^{(\varepsilon_F - \varepsilon_i)/k_B T}) + \sum_{\varepsilon_F \geq \varepsilon_i} (\varepsilon_F - \varepsilon_i) \\
&F^{vib}(V,T) \approx \sum_q^{BZ} \sum_i^{3N} \{\tfrac{1}{2}\hbar\omega_i(V,q) + k_B T \ln(1 - e^{-\hbar\omega_i(V,q)/k_B T})\}
\end{aligned}
\qquad (1)
$$

where $F^{elec}(V,T)$, $F^{vib}(V,T)$, $U^{elec}(V,0)$, and $F^{elec,T}(V,T)$ are electronic free energy, vibrational free energy, internal energy, electronic excitation free energy, ε_F is the Fermi energy, ε_i is the *i*th energy of fermions, $\omega_i(V,q)$ is the round frequency of *i*th branch of bosons at wave vector *q*.

Other thermodynamic properties can also be calculated from the above obtained Helmholtz free energy, for example, entropy $S = -(\partial F/\partial T)_V$, pressure $P = -(\partial F/\partial V)_T$, Gibbs free energy $G=F+PV$, constant volume specific heat $C_V = T(\partial S/\partial T)_V$, volume thermal expansion coefficient $\alpha_V(T)$ =

d{lnV(T)}/dT, isothermal bulk modulus B(T) = -1/(d[lnV(T)]/dP), thermal Grüneisen parameter γ_{th} = $V\alpha_V(T)$ B(T)/C_V, and constant pressure specific heat $C_P=(1+\gamma_{th}\ \alpha_V(T))C_V$.

The G(P,T) package has been successfully used in elastic constants studies of common ceramics[**32**], the prediction of a novel phase of SiO_2 in which a similar supercell approach was applied on modeling solid solution zirconium silicate $(ZrO_2)_x(SiO_2)_{1-x}$[**27, 26**]. More recently similar work has recently been performed on mullite-type lattice of alumina[**28**].

OLCAO

The first principles orthogonalized linear combination of atomic orbitals (OLCAO) method developed by Dr. W.Y. Ching is a very efficient for electronic structure, optical properties, charge and bonding analysis of large complex systems[**33, 34**]. As an all-electron localized atomic orbitals method in complementary to pseudopotential method, OLCAO has the advantage of interpreting electron structure, local bonding and many other properties in terms of local atomic contribution and allows studying core electron related phenomenon. It had been extended to realistically calculate the XANES spectral by including the core-hole effect[**35**].

OLCAO method is especially suitable for electronic structure studies of complex multi-component systems. This is due to the use of atomic basis set and a real space based evaluation of multi-center interaction integrals using a Gaussian transformation technique. The atomistic description of electron states facilitates the interpretation of spectroscopic data for structural and chemical analysis. There is no rigid shape approximation to the potential and charge density distribution even though individual terms in the functional representation consist of spherical Gaussians. Structural analysis is possible via total energy calculation. There are no limitations on the symmetry of the system to be studied or the type of atoms involved.

In the OLCAO method, calculation of effective charges Q^*_α on each atom and the bond order (also called overlap integral) $q_{\alpha\beta}$ between a pair of atoms is a very effective way to quantify the charge distribution, and charge transfer and bond strength in the material. The technique is based on the Mulliken

population analysis scheme and is most effective with a separate minimal basis calculation. These can be obtained according to:

$$\rho_{\alpha,i} = \sum_{n,occ}\sum_{j,\beta} C^n_{i\alpha} C^n_{j\beta} S_{i\alpha,j\beta}\ ; \qquad Q^*_\alpha = \sum_i \rho_{\alpha i}\ . \qquad q_{\alpha\beta} = \sum_{n,occ}\sum_{i,j} C^n_{i\alpha} C^n_{j\beta} S_{i\alpha,j\beta} \tag{2}$$

where n, α, i label the energy state, the atom and the orbital representation respectively, $C_{i\alpha}$ is the eigenvector coefficient and $S_{i\alpha,j\beta}$ is the overlap integral between the Bloch functions. The summations over n include all occupied states and the k-space sampling in the Brillouin zone.

OLCAO method has a strong record to prove its ability to study large and complex systems. It has been applied some of most challenge problems in various fields, for example, amorphous Si[**36**] and SiO_2[**37**], biomolecules Vitamin B_{12}[**38**] and DNA[**39**], integranular thin film in silicon nitride ceramics[**40**], and the Y-Si-O-N solid solution systems[**41**], etc. Its ability to produce reliable XANES/ELNES spectra has been demonstrated in alumina[**35**], silicon nitride[**42**], spinel[**35**], and vitamin B_{12}[**38**], etc. Particularly worth of mention, the OLCAO method had been used to produce XANES finger print which can used to detect highly dilute doping in MgO[**43**].

Software Modules Implemented During the Project Period

We implemented additional automation modules within our G(P,T) package to meet the challenge of carrying out large number of complex first principles calculations required for sufficient sampling of the configuration space using large supercell models for disordered crystals.

Task A1: Supercell Sampling Module (Lead by PI at TSU)

Our goal is to develop software tools that enable us to study disordered crystals for their structures and properties using first principles methods. Most first principles methods for condensed matter require period structure. To properly represent the local structure variation in disordered system, large supercell models are needed. To facilitate supercell model calculations, we developed the supercell sampling module that is capable of: (1) generate supercell model based on common crystal structure description

formats such as CIF in which partial occupations are used to direct the construction of the supercell model; (2) automated large number of similar supercell calculations using one simple common input setting.

We have implemented two methods to generate supercell models for crystal lattices with substitution disorder: (1) randomly placing atoms at lattice points and interstitial sites; (2) randomly placing unit cells of different carbon configurations in the supercell. The first approach is straightforward but lattice points and interstitial sites are static and should be predefined. The second one can be more flexible since topology inside the cell can be different but requires unitcells to share corners and facets. We also implemented a symmetry analysis module to detect models with high symmetries.

The main challenge is to obtain physical properties of the disordered system from large number of supercell calculations which each calculation can be computationally intensive. There are few approaches with reasonable prediction capability for studying thermodynamic properties of disorders crystal using first principles methods including exhaustive sampling in a large supercell space, genetic algorithm or Monte Carlo simulation in supercell space, and cluster expansion method. The latter approach is based on rigorous theory has been the popular approach to study disordered crystal. Cluster expansion method with energy expressed in a finite maximum cluster basis set can achieve reasonable accuracy at modest computational cost for simple structures.

Exhaustive sampling even in the smallest 2x2x2 boron carbide supercell space can be computational prohibitive as it requires first principles calculations of a 120-atom structure for about $C_{120}^{N_C}$ times where N_c is the number of carbons, although symmetries can exploited to reduce the number of calculations in a rather limited scale. To accelerate the searching for minimal energy configurations and the calculations of thermodynamic properties, we have implemented optimized sampling method including genetic algorithm and Monte Carlo method. For both methods, a lattice site level swap and a unitcell level swap were implemented. For the lattice site level swap, each step in genetic algorithm and Monte Carlo method selected lattice site or sites are swapped, while for the unitcell level swap, selected unitcell or unitcells are swapped.

We also explored the cluster expansion method for physical properties calculations of disordered lattices. Cluster expansion method for complex multi-sublattice crystal was developed by Ceder *et al* in 1995. While the cluster expansion of a simple single sublattice can be considered as a Taylor expansion of one discrete site occupation variable, they propose to use a multivariable Taylor expansion for multi-sublattice crystal in which each sublattice is treated as an independent site occupation variable. Direct application of Ceder's approach to boron carbide with 15 sublattices would be computationally prohibitive since even for simple up to near-neighbor cluster expansion, it requires number of cluster interaction parameters up to 15^4.

In traditional cluster expansion method, the energy was expressed in terms of atomic clusters. In practices, a maximum complete cluster set γ is used as cut off in the energy expression,

$$E(\vec{\sigma}) \cong \sum_{\alpha \in \gamma} V_\alpha \Phi_\alpha(\vec{\sigma}) \tag{3}$$

where $\vec{\sigma} = \langle \sigma_1, \sigma_2, \cdots, \sigma_N \rangle$ is the configuration vector, α is a cluster in γ, σ_i is the site occupation variable at ith lattice site, V_α is the effective cluster interaction coefficient, and $\Phi_\alpha(\vec{\sigma})$ is the cluster function of cluster α. The above approach has been extensive used to study binary alloys. However, if the lattice is complex and many non-equivalent lattice sites existed in the structure, the traditional cluster expansion method can be computationally expensive if not prohibitive. In the case of boron carbide, where carbon atoms could reside randomly on the stable conjugated icosahedra, the maximum cluster can be exceedingly large as huge maximum cluster set with clusters up to 12 atoms may be needed.

We propose to express the energy of the disordered crystal in terms of primitive unitcell, therefore we call it unitcell expansion method (UEM),

$$E(\vec{\eta}) \cong \sum_{\beta \in \varsigma} V_\beta \Phi_\beta(\vec{\eta}) \tag{4}$$

where ζ is the maximum complete cluster set of unitcells, β is a cluster in ζ, $\vec{\eta} = \langle \tau_1, \tau_2, \cdots, \tau_L \rangle$ is the configuration vector, $\tau_i = \tau\left(\sigma_1^{(i)}, \sigma_2^{(i)}, \cdots, \sigma_{n_i}^{(i)}\right)$ is ith unitcell configuration variable, V_β is the

effective unitcell cluster interaction coefficient, and $\Phi_\beta(\vec{\sigma})$ is the unitcell cluster function of cluster β. Energy expansion in terms of unitcells trades the complexity in lattice for increased component types. For one unique site simple lattice such as BCC/FCC, UEM reduces to traditional cluster expansion method. For complexity lattice, particularly large unitcells, UEM has significant advantages. First, it is possible to reduce the number of unique unitcell types, $\boldsymbol{n}_\tau$. For a given concentration, we can carry out an extensive in unitcell or small supercell calculations to identify the lowest configurations that will be used in the UEM calculations. Second, if the unitcell is large enough, it is possible only small clusters up to near-neighbor clusters or at most triplets will be needed in the energy expression, thus the total number of effective cluster interaction coefficients (ECI) $N_{\boldsymbol{\beta},\mathbf{n}_\tau}$, remains manageable (~$\boldsymbol{n}_\tau^{2\sim3}$). Third, it is quite simple to introduce lattice defects, surface structures in this approach.

If only considering the nearest neighbor interaction, the UEM becomes a Potts model. Potts models is a generalized Ising model in which a finite set of symbols, here we referred as unique unitcell types, is used to defined to the lattice site occupations,

$$H_g = -\sum_{(i,j)} J_{ij}\boldsymbol{\delta}(\boldsymbol{\tau}_i,\boldsymbol{\tau}_j) - \sum_i h_i\boldsymbol{\tau}_i \qquad (5)$$

where J_{ij} is the near-neighbour interaction, h_i is the self-interaction energy coefficient of *i*th lattice site.

The UEM module implemented within the G(P,T) package consists four programs: (1) a small supercell sampling program to generate configurations for fitting the ECIs; (2) a parallel job manager for effectively running on high performance computers; (3) a constrained fitting program for extracting the ECIs; (4) simulation program using Monte Carlo method or genetic algorithm to calculate configuration free energy for a given composition.

Task A2: G(P,T) Interfaces to OLCAO Package (Lead by Dr. Ching at UMKC)

We have implemented module that interface G(P,T) to the OLCAO package that enables the whole process of the OLCAO calculation from input generation to output analysis to be managed as a G(P,T)

task similar to phonon calculation. A set of corresponding analysis and visualization tools was developed for post-process of OLCAO calculations.

Task A.3: Supercell Statistics Module (Lead by PI at TSU)

In this task, we will develop a supercell statistics module to compute free energy and other properties from supercells sampled. Retrieving properties from an ensemble average can be a nontrivial task. Energy can be calculated directly with sufficient accuracy only from an ensemble average based on sampling of sufficiently large supercell models. For cluster expansion approach, however, free energy has to be obtained from the Monte Carlo simulation of larger supercell models whose free energies are empirically estimated from local clusters it is made of. Other properties such as mechanical properties and thermal expansion coefficient, however, have not been attempted as far as we know. One way to calculate them is that by assuming large supercells of nanometer size behaves like crystallites, which could be arguably suitable for covalent material, methods such as the Voigt-Reuss-Hill method[**44**] developed for polycrystalline materials which can then be applied.

Beyond

We implemented a pressure dependent elastic constants calculation module. Ab initio force calculations are the bases for theoretical evaluation of mechanical, elastic and vibrational properties. In the G(P,T) package, the elastic constants C_{ij}(P,T=0) at a given pressure P are calculated from the following equation,

$$C_{ij}(P,T=0)=\left.\frac{\partial^2 U(\{e\})}{\partial e_i \partial e_j}\right|_{\frac{\partial U(\{e\})}{\partial e_i}=-P\lambda_i} \quad \text{where } \lambda_i=\begin{cases}1, i=1,2,3\\ 0, i=4,5,6\end{cases} \tag{6}$$

where U({e}) is the total energy of a given periodic structure represented by a strain $\{e\}$ relative to a reference structure.

To calculate the elastic constants C_{ij}(P,T=0), U({e}) has to be evaluated in a six dimension strain parameter space, which can be computationally prohibitive if the full parameter space is to be explored. If only elastic constants at hydrostatic pressures are to be calculated, the computational complexity can be greatly reduced since the total energy calculations are limited to the strain space within the proximity of the structures under hydrostatic pressures. We calculate the hydrostatic pressure and elastic constants in the following steps. (1) A zero temperature equation of state is calculated to estimate the periodic cell volume range corresponding to the targeted pressure range. (2) A series of structures covering the volume range estimated from the targeted pressures are first optimized at zero temperature as the reference structures $\{e\}_0^k$ where *k* is the index of the reference structure. (3) A set of strains in the form of $x\sum_{i=1,6} a_i \hat{e}_i$, where *x* is a small factor, a_i is a constant, and $\hat{e}_i$ is the strain basis, are applied to the reference structure. The total energies of the strained structures $\{e\}_j^k$, where *j* is the index of strain, are calculated using the total energy module in the G(P,T) package. Symmetry is explored to reduce the number of strains and to maintain as higher symmetry as possible in the strained structure. (4) The obtained total energies of the strained structures $U(\{e\}_j^k)$ are used to fit against the free energy model,

$$U(\{e\}_j^k) = U(\{e\}_j^k) - V(\{e\}_j^k)\boldsymbol{\sigma}(\{e\}_j^k)\boldsymbol{\varepsilon} + 1/2V(\{e\}_j^k)\boldsymbol{\varepsilon}C(\{e\}_j^k)\boldsymbol{\varepsilon} + O(\boldsymbol{\varepsilon}^3) \qquad (7)$$

where $V(\{e\}_j^k)$, $\boldsymbol{\sigma}(\{e\}_j^k)$, and $C(\{e\}_j^k)$ are the volume, strain, stress and elastic constants tensors, $O(\boldsymbol{\varepsilon}^3)$ is the higher order error term. From the free energy model, we locate the strained structure $\{e\}_P^k$ with hydrostatic pressure P^k on the energy surface. For a quadratic energy model, we have:

$$V(P^k)C(P^k) = V(\{e\}_P^k)C(\{e\}_P^k) = V(\{e\}_0^k)C(\{e\}_0^k) \quad (8)$$

assuming $\{e\}_P^k$ is at the close proximity of $\{e\}_0^k$. It is possible to include higher order terms in the total energy model but the computational costs will be significantly larger since much more parameters will be included in the total energy model. Step 4 is repeated for each reference structure to obtain the pressure dependent $C_{ij}(P^k)$. This approach as implemented in the G(P,T) package can be applied to any symmetry type of solids.

Details about the calculations

G(P,T) package employs Vienna *ab initio* package (VASP) for energy and force evaluation. The accuracy settings used for supercell sampling are: (1) the planewave energy cutoff is at 400eV; (2) the convergence is at 10^{-7} eV and 10^{-3} eV/Å for energy and force, respectively; (3) A 2x2x2 supercell which consists of 120 atoms is used for phonon calculation. A 20x20x20 K-point mesh is used for Brillouin zone integration of density of states. No LO/TO splitting is included.

IV. Results and Discussions

Carbon distribution in Boron carbide

We sampled more than 800 2x2x2 supercells to estimate the carbon distribution in boron carbide for composition with x=0. 24 carbon atoms were randomly placed on the 120 sites supercell. Note that the supercell sampling is limited to unitcells without defects such as vacancies and interstitial occupations. Supercells were relaxed with cell parameters fixed. Figure 2 shows the energies distribution of the sampled supercells. The Gaussian-alike distribution with peak at 7.725eV/atom and the small variance of per atom energy of about 30meV. From the ideal

solid solution theory, we estimate the entropy contribution to the free energy at formation temperature of 3000K to be 140meV. This clearly indicates that carbon distribution in boron carbide is random. **Therefore no further work on symmetric supercell was pursued**.

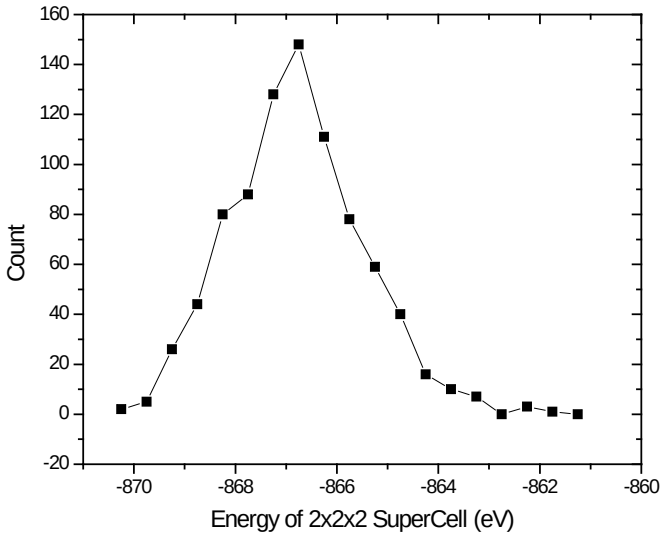

Figure 2. Energy distribution of the sampled 2x2x2 supercells

Figure 3 shows the pressure distribution of the sampled supercells. The pressures are dominantly located at low pressure region of -1GPa to +1GPa. Therefore, the elastic energy contribution is orders of magnitude smaller that that of entropy thus trivial in present calculations.

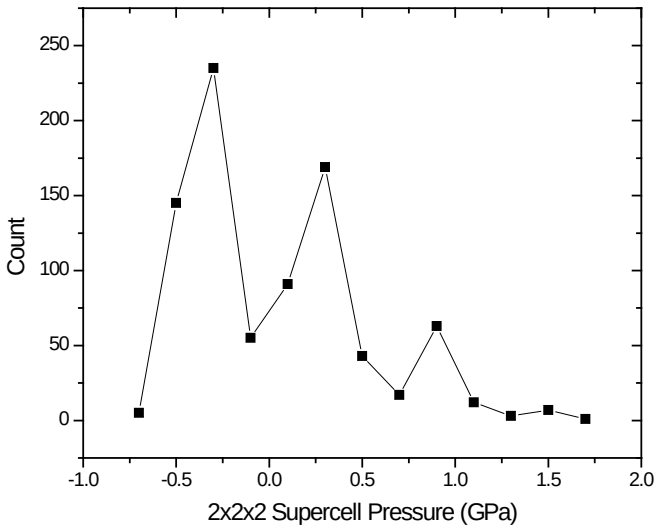

Figure 3. Pressure distribution of the sampled 2x2x2 supercells.

We can further compute the carbon distribution in the supercell using the following formula,

$$\chi_i \approx \sum_s \exp(-E_s / k_B T) * X_{i,s} \qquad (6)$$

where $X_{i,s}$ is the occupation variable (1 for carbon and 0 for boron) of *i*th site of *s*th supercell sample, E_s is the supercell energy, and T is the temperature. At T=2000K, the estimated carbon sites occupations are characterized as: **(1) the two end sites of the 3-atom chain is almost completely occupied; (2) about 2% of carbon will be located at the center of the 3-atom chain; (3) the remaining 98% will be located on the 12-atom icosahedrons**.

We also applied the unitcell expansion method to study the physical properties of boron carbides. The 15-atom primitive unitcell has been used to expand the energy of an infinite crystal. There will be about 2^{15}= 32768 possible configurations if carbon is allowed at all sites in the 15-atom rhombohedra primitive unitcells. For feasible unitcell expansion method calculation, it is necessary to reduce the candidate unitcell configurations. To screen for candidates unitcell, we

carried out exhaustive search for all possible unitcells with carbon concentration x ($B_{12-x}C_{3+x}$) that are not too far from the interested one.

Figure 4 plots the energy and pressure of all possible unrelaxed primitive unitcell with x=-2. The red symbol indicates sites on the ends of the 3-atom chains and black symbol indicates otherwise. The energy gap between the lowest two unitcells is about 0.5eV/atom which clearly indicates for unitcell with only 1 carbon, the carbon will go to the ends of the 3-atom chains. Thus only two such unitcells are included in our unitcell candidates set.

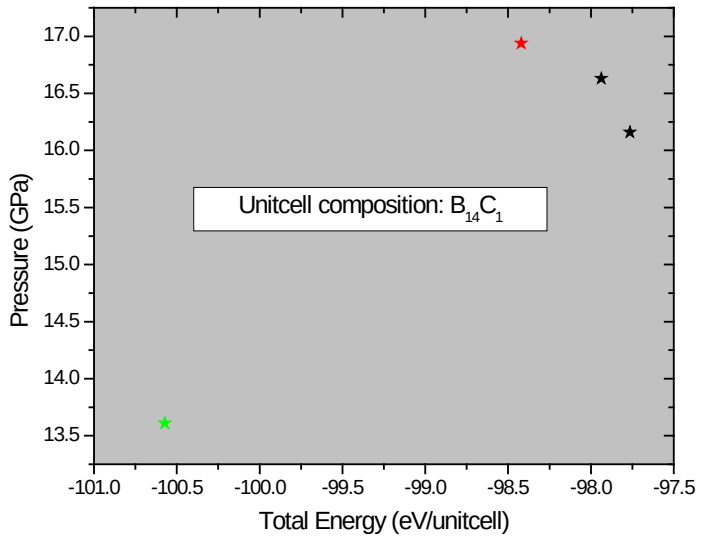

Figure 4. Total energy and pressure plot of unrelaxed primitive cell $B_{14}C_1$.

Figure 5 plots the energy and pressure of all possible unrelaxed primitive unitcell with x=-1. The yellow symbol indicates carbon atoms occupy the two end sites of the 3-atom chains. The energy gap between the lowest two unitcells is about 1.4eV/atom which clearly indicates for unitcell with only two carbons, the carbons will go to the ends of the 3-atom chains. Thus only one such unitcell is included in our unitcell candidates set.

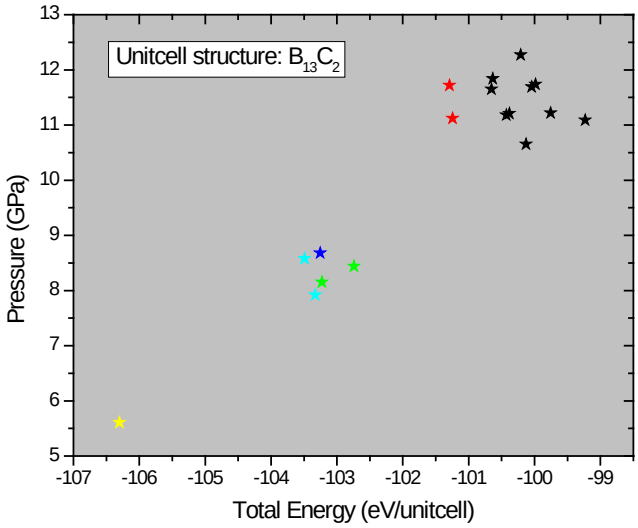

Figure 5. Total energy and pressure plot of unrelaxed primitive cell $B_{13}C_2$.

Figure 6 plots the energy and pressure of all possible unrelaxed primitive unitcell with x=0. The yellow symbol indicates carbon atoms occupy the two end sites of the 3-atom chains and one carbon resides on the equatorial sites of the icosahedron. The energy gap between the group of yellow symbols and the rest is about 0.5eV/atom. We included the six unitcells with 1 carbon on the equatorial sites and one unitcell with all three carbon atoms go to the 3-atom chain..

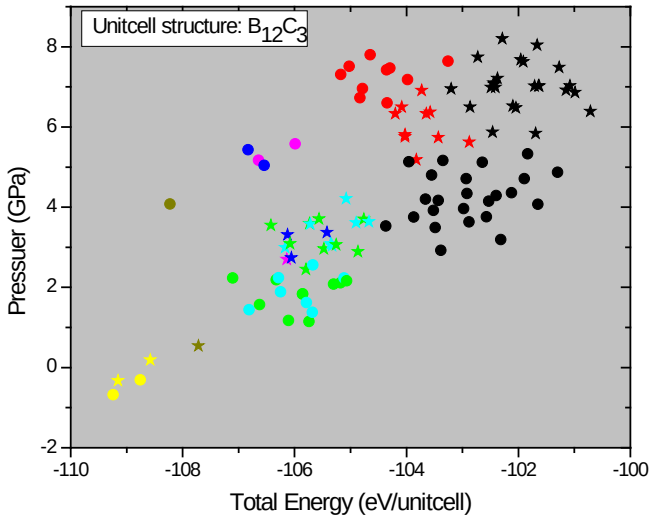

Figure 6. Total energy and pressure plot for all unrelaxed primitive cell $B_{12}C_3$.

Figure 7 plots the energy and pressure of all possible unrelaxed primitive unitcell with x=1. The dark yellow symbol represents unitcell configuration with 3 carbons on the 3-atom chain and 1 carbon on the equatorial sites. The yellow symbol indicates 2 carbon atoms occupy the two end sites of the 3-atom chains and 2 carbon atoms occupy the equatorial sites. The lowest two groups are separated by energy and pressure. However, the energy and pressure showed overlaps between edge members of the two groups. To limit the size of unitcell candidate set, we selected only the lowest members of the dark yellow and yellow group. Note that each symbol may have several symmetry-equivalent models.

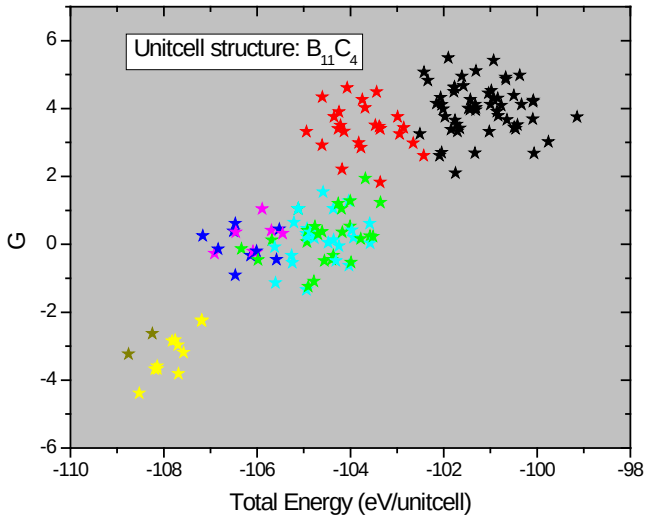

Figure 7. Total energy and pressure plot of all unrelaxed primitive cell $B_{11}C_4$

Figure 8 plots the energy and pressure of all possible unrelaxed primitive unitcell with x=2. The dark yellow symbol represents unitcell with carbon configuration of all 3-atom chain occupied and remaining 2 carbons occupy the equatorial sites. Yellow symbol represents carbon atoms occupy the two end sites of the 3-atom chains and 3 equatorial sites. . Similar to the x=1 case, the lowest two groups are separated by energy and pressure. However, the energy and pressure showed overlaps between edge members of the two groups. To limit the size of unitcell candidate set, we selected only the lowest members yellow group to be included in the candidate set. Note that each symbol may have several symmetry-equivalent models.

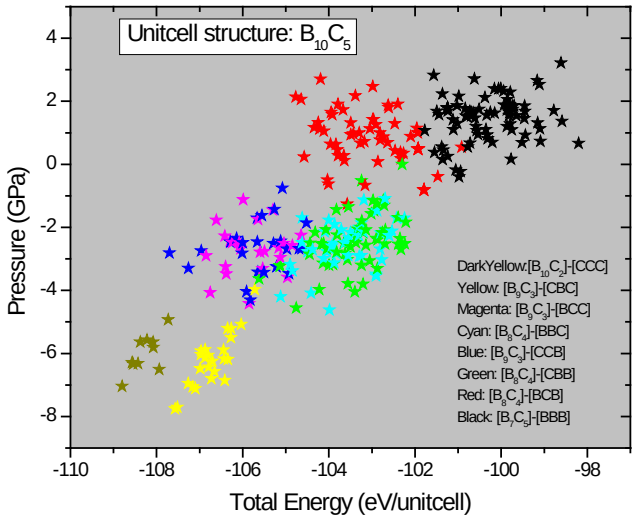

Figure 8. Total energy and pressure plot of all unrelaxed primitve cell $B_{10}C_5$.

To examine the general trend in the carbon site occupation, we plots the energy and pressure of all possible unrelaxed primitive unitcell models with 1 to 5 carbon atoms which correspond to 6.67% to 33.3% in Figure 9. The color indicates the structure of the 3-atom chain. The shapes of the symbols, up triangle, right triangle, diamond, left triangle, and down triangle, correspond to primitive cell structures with x=-2,-1,0,1,2, respectively. The colors of the symbols, dark yellow, yellow, magenta, cyan, blue, green, red, and black, represents C-C-C, C-B-C, B-C-C, B-B-C, C-C-B, C-B-B, B-C-B, and B-B-B, respectively. Clearly the C-C-C and C-B-C are the energetically favored 3-atom chain configurations for all allowable range of x. When there is only one carbon in the unitcell, it prefers to reside at either end of the 3-atom chain. Note that for all unitcell calculations, the experimental unitcell parameters are used.

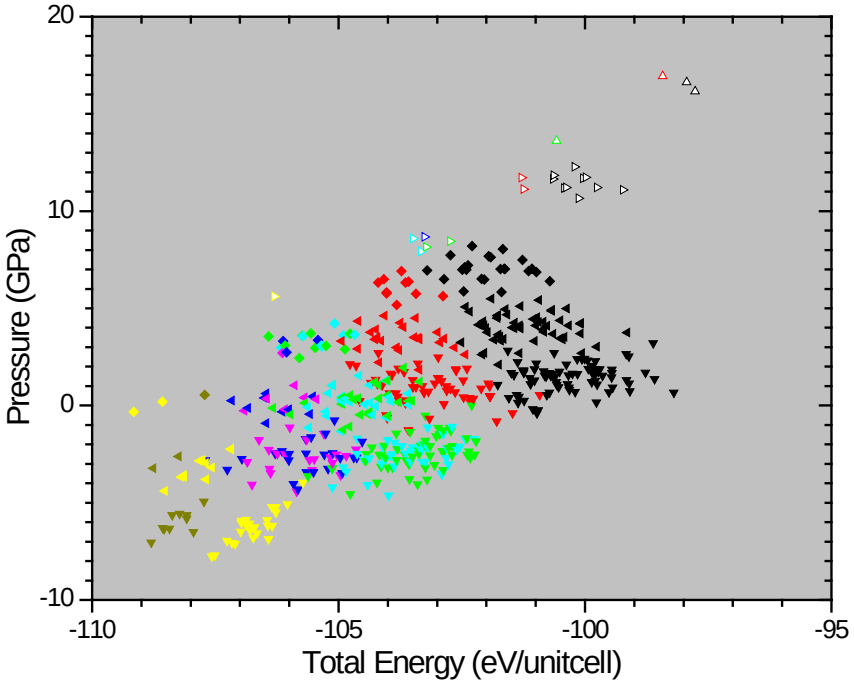

Figure 9. Total energy and pressure plot of un-relaxed $B_{12-x}C_{3+x}$ primitive cells with x=-2,-1,0,1,2.

We also the lowest energy of unrelaxed primitive unitcell models with 1 to 5 carbon atoms. Note the convex shape near x=0. It appears that these lowest primitive unitcells are all stable at least for the low carbon concentrate end.

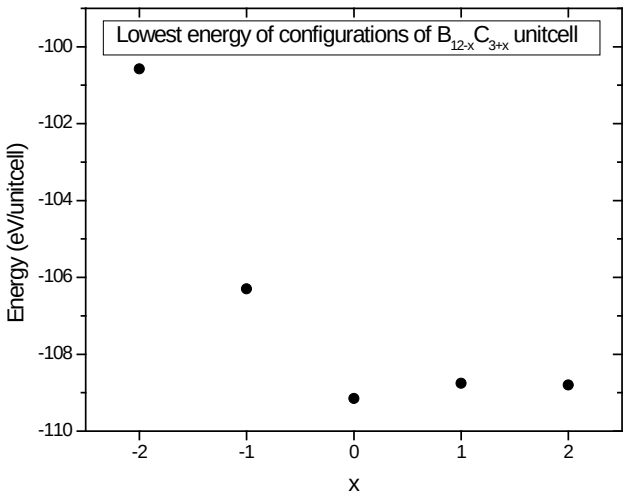

Figure 10. Lowest energies of unrelaxed primitive cells $B_{12-x}C_{3+x}$ with x from -2 to 2.

With the unitcell candidate set defined, we used the UEM module in G(P,T) to study the carbon concentrate dependent free energy of the boron carbide system. Due to limit of computational resources, the candidate unitcells are selected only from the lowest energy configurations for $B_{12-x}C_{3+x}$ with *x* ranging from -2 to 0. The total number of unique unitcells used in the calculation is 9. Because of the rhombohedra primitive unitcells, we considered three types of nearest neighbors in the unitcell expansion: face-shared, edge-shared, and corner shared. The total number of irreducible effective cluster (unitcell) interactions are 85 which were obtained from more than 200 2x2x2 supercell calculations. Figure 11 shows the concentration dependent carbon distribution in boron carbide.

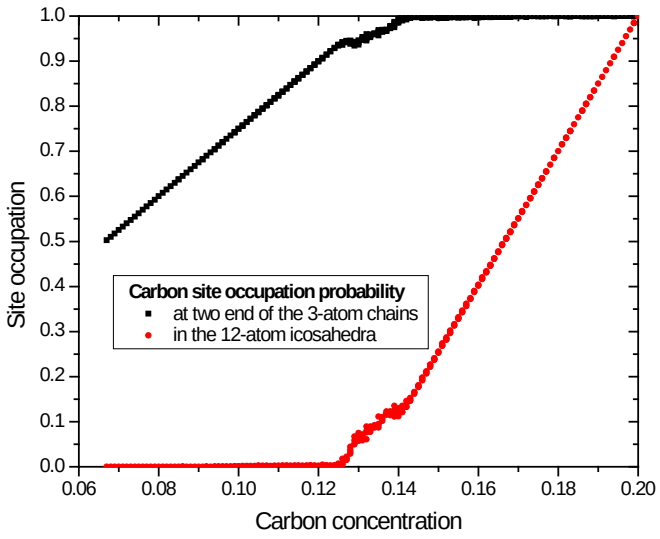

Figure 11. Concentration dependent site occupation in boron carbide $B_{12-x}C_{3+x}$

Because of the restricted unitcell candidate set, the result at x=0 gave no carbide occupation on the center of the 3-atom chain. However, since the trend is what we seek here, we ignore the small discrepancy from the supercell sampling. Figure 11 clearly showed a gradual loss of carbon all exclusively from the icosahedrons as x goes from 0 to -1. Near x=-1, we see a noisy transition from loss on icosahedrons to loss on the 3-atom chains, which corresponds to the observed change of physical properties near concentration of 13%. However, we did not observe the distinct structural change near 8%

which also showed distinct change of physical properties from experiments. This suggested more unitcell might be needed if there indeed has structural change or possibly electronic structure change may also contribute to the cause. Further properties calculations will be needed to if a distinct structural changes happened near 8% carbon concentration of boron rich boron carbide.

Boron Carbide and Related Compounds

We systematically studies boron and boron compound to better understand their structural-properties relation. Elastic properties, electronic structure, charge-bonding, vibrational properties, and XANES are calculated for boron, boron carbide, and boron oxide.

The structural data of these three crystals are listed in Table I. The most prominent feature is the 12-atom icosahedra with polar and equatorial sites with the intra and inter-icosahedral bonds. Each B_{polar} atom has six intra-icoshedral bonds and one inter-icosahedral bond which is shorter than the intra-icosahedral bond. This was the main argument that these crystals are inverted molecular solids. Each B_{equal} atom in α-B_{12} has only five intra-icosahedral bonds and no inter-icosahedral bond. In B_4C and $B_{12}O_2$, the B_{equat} also has one short bond with the atom in the chain or O. The key difference in these three crystals is the presence of chain atoms along the rhombohedral body diagonal in B_4C and $B_{12}O_2$. This resulted in the general observation that the B-B distances in a-B_{12} and $B_{12}O_2$ are comparable, and both are shorter than that in $B_{11}C$-CBC. In B_4C, the middle B atom in the three-atom chain has two short bonds of only 1.429 Å to the other two C atoms which are bonded to the B_{equat} atoms. In $B_{12}O_2$ the two O atoms are not in the form of a “chain” since they are well separated at 3.01 Å and are not consider to be bonded. Both O atoms in $B_{12}O_2$ and the end atoms in the chain in B4C are bonded with three B_{equat} atoms in three neighboring icosahedra. The O-B_{equat} BL is relative short (1.493 Å).

Table I. Crystals structure parameters of α-B_{12}, B_4C, and $B_{12}O_2$. Bond lengths are in Å.

Crystal	α- B_{12}	B11C-CBC	$B_{12}O_2$
a(Å)	4.9888	5.1651	5.1346
α(˚)	58.063°	65.705°	63.164°
Atoms/cell	12	15	14
Different atomic sites	2	4	3
B_p-B_p	1.656*, 1.725(2)	1.715*, 1.809(2)	1.691*
B_p-B_e	1.778(2)	1.787, 1.802(2)	1.777(2)
B_e-B_e	1.760(2)	1.762 (2)	1.751(2)
B_p-C_p	-	1.715*, 1.809(2)	-
B_e-C_p		1.787, 1.802(2)	
B_e-C_c	-	1.606	-
B_c-C_c	-	1.429	-
B_e-O	-	-	1.493
O-O	-	-	3.01

* Inter-icosahedral bonds; p. Polar; e. Equatorial; and c. Chain.

Elastic Properties

The mechanical properties of boron and born compounds are central to many of their applications. Table II list the calculated elastic constants and bulk elastic properties of the α-B_{12}, B_4C and $B_{12}O_2$ crystals. The elastic constants of B_4C and $B_{12}O_2$ are comparable, both larger than that of a-B_{12}. This is in line with the claims that they are the third hardest materials after diamond and cubic boron nitride. Our results also show that they have similar mechanical strength in terms of bulk, shear and Young's moduli. Although α-B_{12} has never been mentioned as a super-hard material, it also has quite large elastic constants and bulk moduli. It is noted that the C_{44}, C_{55} and C_{66} values of α-B_{12} are actually larger than that of B_4C and $B_{12}O_2$, which seems to indicate that α-B_{12} is stiffer in certain directions than B_4C and $B_{12}O_2$ and that has resulted in a large shear modulus G for a-B_{12}. The calculated Poisson ratio for α-B_{12} (0.14) is smaller than that of B_4C and $B_{12}O_2$ (0.18). This implies that α-B_{12} is relatively more compressible than the other two crystals. This could be attributed to the absence of chain atoms in a-B_{12}. However, experimental measurements and theoretical calculations of the elastic properties on these three crystals are rather limited. Most of them reported only the isotropic elastic bulk modulus. These include the work of Nelmes *et. al.* [19] measured bulk modulus of α-B_{12} using single crystal x-ray technique. Lazzari *et. al.* [9] did the calculations on bulk modulus of α-B_{12} and B_4C as well as the infrared and Raman spectra of B_4C for different atomic configurations and compared with available experimental spectra. They have concluded that the $B_{11}C$-CBC structure with one C at polar site and the three-atom CBC chain is the most likely structure of the B_4C. Our calculated bulk modulus K= 228.1 GPa for α-B_{12} is in very close agreement with the measured value of 224 GPa by the Nelmes *et.al* and the theoretical value of 222 GPa by Lazzari *et al.*. For B_4C our calculated value of K= 251.5 GPa is larger than the 215

GPa reported by Zhang from shock compression measurement and only slightly larger than the theoretical value of 248 GP. On the other hand, our value is in excellent agreement with the data of K= 247.0 GPa by Gieske et. al. from the ultrasonic velocity measurements . Similar good agreement with Dodd et al using ultrasonic measuremhaent at 295K has been obtained. An interest obersvation is that the data of McClellan et al on $B_{5.6}C$ samples gave K = 236.8 GPa which is only slightly smaller than that of B_4C. In the case of $B_{12}O_2$, our calculated bulk modulus of 252 GPa is slightly larger than the measured value of 230 GPa by Petrak et al by about 9% whereas our calculated Young's modulus of 480 GPa is very close to the measured value of 476 GPa. Guo et al has obtained a theoretical bulk modulus value of 237 GPa for B12O2 smaller than what we calculated. These comparisons of calculated and measured data on the emhcnaical properties essentially show that they are very much depedent on the actual samples used and the type of experiments conducted. Our calculated values refer to perfect crystals within hte limitations of the usual density functional theory.

Table II. Calculated elastic constants (C_{ij}), bulk modulus (K), shear modulus (G), Young's modulus (E) and Poisson ratio (η) in the three crystals. Cij is in unit of GPa.

System	C_{11}	C_{22}	C_{33}	C_{44}	C_{55}	C_{66}	C_{12}	C_{13}	C_{14}	C_{23}
α-B_{12}	567.2	567.2	516.2	182.5	182.5	244.4	78.5	62.2	22.2	
B_4C	597.7	584.5	550.6	169.1	173.3	224.9	129.1	73.8	-----	68.0
$B_{12}O_2$	592.8	592.8	459.1	180.8	180.8	236.2	120.4	48.7	21.4	-----

System	**K** (GPa)	**G** (GPa)	**E** (GPa)	**η**
α-B12	228.1 224.0[a] 222.0[b]	214.5	490.0	0.14
B_4C	251.7 247.0[c] 248.0[b]	206.2 200.0[c]	485.9 472.0[c]	0.18 0.18[c]
B12O2	252.0 230.0[d]	203.0	480.0 476.0[d]	0.18

a,b,c,d from ref. 9,19.

Electronic Structure

The electronic structure and bonding of the elemental B, B_4C and boron compounds have been extensively studied for more than 20 years both experimentally and theoretically. Extensive calculations using plane wave pseudopotential method have been done by Lee and coworkers [49]. Li et al used the same OLCAO method as in the present work to study the band structure and optical properties of elemental B, B_4C and $B_{12}O_2$ using experimentally determined crystal structure more than 15 years ago. The present calculations are the extension of these earlier works with much higher precisions. Other relevant work related to the electronic structure and spectroscopic properties include those of Fujimori et. al. who measured distributions of electron density in α-B_{12} using synchrotron radiation; Zhao et. al. who studied theoretically on the changes in band structure of α-B_{12} with pressure and found that at high pressure around 160 GPa α-B_{12} becomes metallic. XANES/ELNES spectroscopic data on these boron and boron compounds have been reported by many groups.

The electronic structure and the optical properties of α-B_{12}, B_4C and $B_{12}O_2$ crystals are calculated using the OLCAO method. Figure 12 shows the calculated band structures which are quite different from each other especially in the valence band (VB) region. They are all semiconductors with indirect band gaps of 2.61, 2.97, 2.94 eV and direct band gaps at Γ-point of 3.30, 5.04 and 5.44 eV respectively for α-B_{12}, B_4C and $B_{12}O_2$. The actual band gap values may be somewhat larger than the calculated values since LDA generally underestimates band gap. These calculated band gaps are consistent with other recent calculations. The calculated total DOS (TDOS) and partial DOS (PDOS) for α-B_{12}, B_4C and $B_{12}O_2$ are shown in Figsure 13, 14 and 15 respectively which show very different features among the three crystals. In a-B12, the VB consists of three segments, the two lower segments (-16.9 eV, and from -13.3 -11.8 eV) are

similar for B_{polar} and B_{equat} but are quite different for the upper segment (-9.9 to 0.eV) which involves the B 2p orbitals in the three center bond. The top of the VB consist of states mostly from B_{polar}. In the CB region, the TDOS has highly pronounced peaks below 10 eV which will be reflected in the XANES spectrum to be discussed below. The lower part of CB is mostly dominated by B_{equat} and the upper part by B_{polar} whereas middle part has almost equal contribution from both sites.

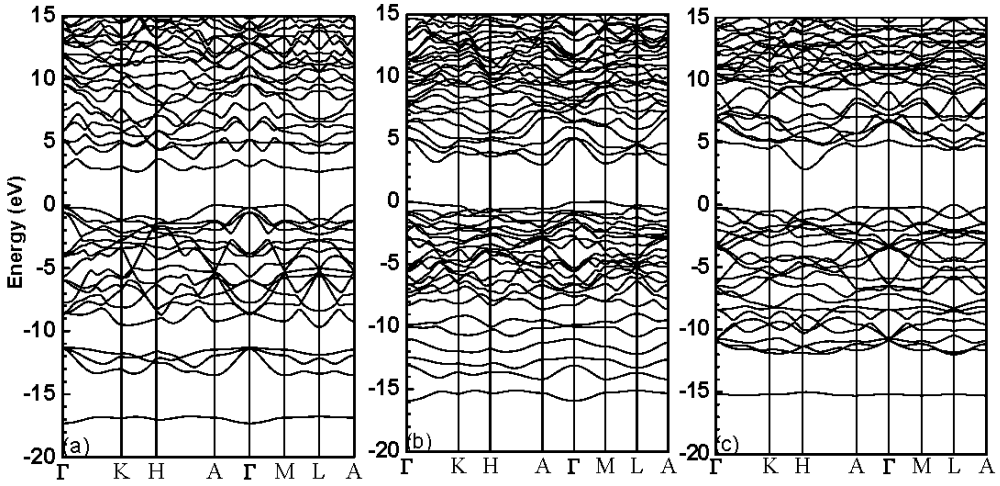

Figure 12. Calculated band structures of: (a) α-B_{12}, (b) B=C and (c) $B_{12}O_2$. The top of the VB is set to zero.

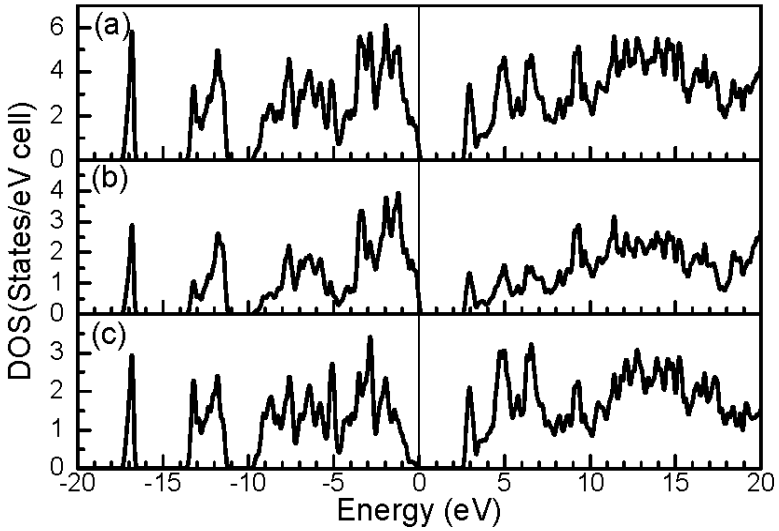

Figure 13. **Calculated total DOS and PDOS of α-B_{12}. (a) Total; (b) Bpol; (c) Bequat.**

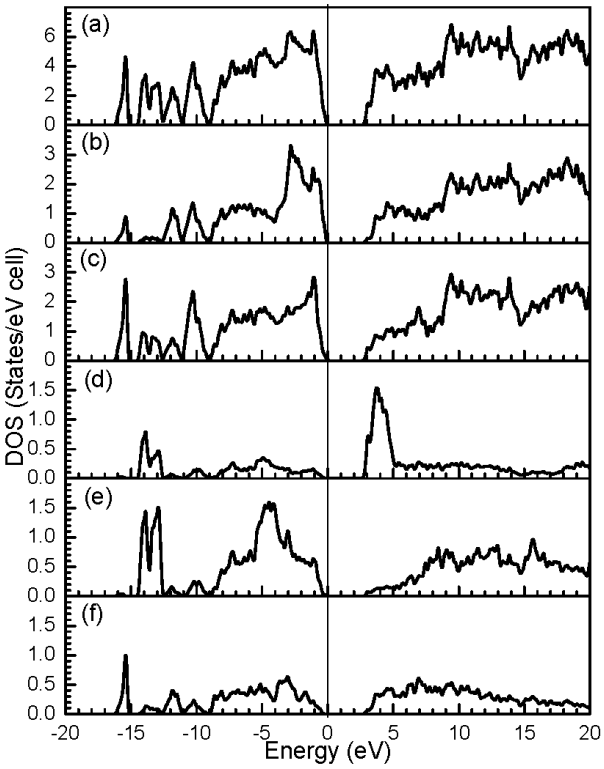

Figure 14. Calculated total DOS and PDOS of B4C. (a) Total; (b) Bpol; (c) Bequat; (d) B in the chain; (d) C in the center of the chain; (e) C in the icosahedron at the polar site.

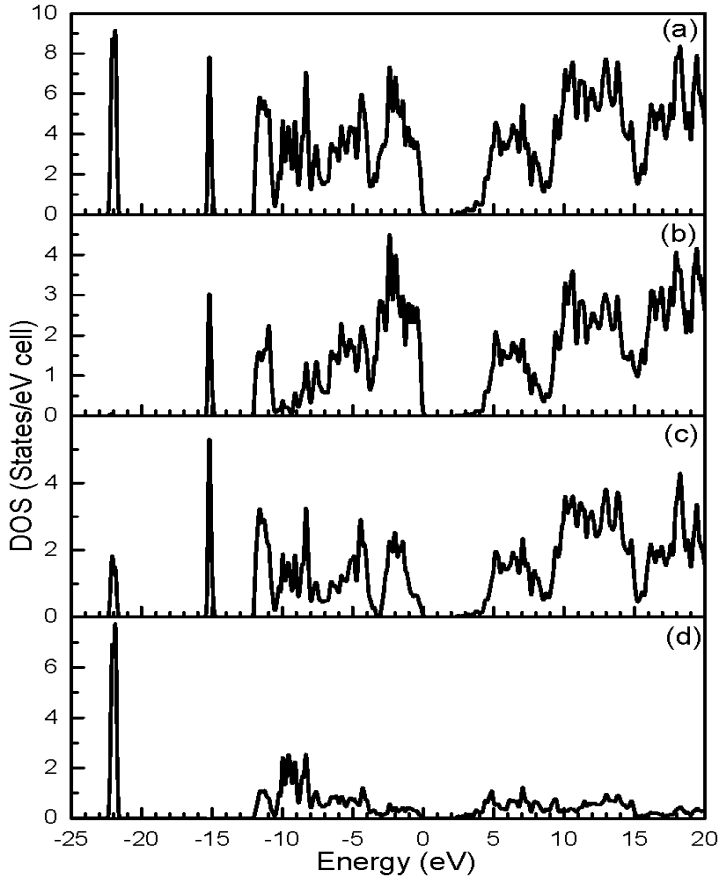

Figure 15. Calculated total DOS and PDOS of $B_{12}O_2$. (a) Total; (b) Bpol; (c) Bequat; (d) B in the chain; (d) C

The TDOS in the VB region of B_4C is quite different from that of a-B_{12}. The lower and upper segments are not well separated. The lower part of the TDOS has multiple peaks while the upper part is quite broadened. These differences come from the presence of the B-C-B chain atoms. The chain C atoms have significant contribution to the in middle region of the lower VB and the middle part of the upper VB. In the CB region of B_4C, B_{equat} and B_{polar} have similar CB DOS features and the central B in the C-B-C chain dominates the lower part of the CB which will again be reflected in the special features in the XANES spectrum.

In $B_{12}O_2$ the lower VB TDOS has two highly pronounced peaks. The peak at -21.9 eV is from O 2s which interact with B_{equal}. The other peak at -15.2 eV is from B_{equal} and B_{polar} similar to that in a-B_{12}. In the upper VB region, the TDOS has several well defined peaks with the lower portion from O 2p orbitals and the upper portion from B-2p orbitals. We have noted that the width of the upper VB in a-B_{12} (9.97 eV) is larger than that of B_4C (9.05 eV), both are much smaller than that in $B_{12}O_2$ (12.32 eV). In the CB region below 10 eV, there are no prominent peaks as in the a-B_{12} due to the presence of the O ions. Above 10 eV, the DOS is similar to that of a-B_{12}. Such differences in the CB DOS will be clearly reflected in very different XANES spectrum to be discussed below.

The interband optical transition spectra of α-B_{12}, $B_1$1C-CBC and $B_{12}O_2$ crystals were also calculated using the OLCAO method. Such calculations become quite routine and have been described in many papers and will not be repeated here. Basically, the electronic structure is calculated using an extended basis with the fully converged potential at a large number of k-points within the BZ. The dipole matrix elements of transition from the VB states to the CB states are evaluated and the transition rate (or the imaginary part of the dielectric function

$\varepsilon_2(\hbar\omega)$) is calculated within the random phase approximation by summation over the BZ up to high photon energy of about 40 eV. The real part of the dielectric function $\varepsilon_1(\hbar\omega)$ is then obtained from $\varepsilon_2(\hbar\omega)$ by Kramers-Kronig conversion. The calculated results in the form of complex dielectric functions for the three crystals are shown in Figure 16. All three crystals have multiple sharp absorption peaks within the first 8 eV range from the edge on set reflecting the complex peak structures of the crystals both in the VB and in the CB. These results are close to those obtained before using the same method except in accuracy is much more improved. There are many peaks structures in the $\varepsilon_2(\hbar\omega)$ in the three crystals. However the centers of the main absorption peaks in these three crystals all lie within the range of 6.6 eV to 7.1 eV, indicating the overall absorption spectra are dictated by the icosahedral B units. We have also resolved the optical transitions into components in the direction parallel to the axial direction of the rhombohedral cell and perpendicular to that direction. The results are shown in Figure 17. The reflective index n of the crystal can be obtained as the square root of $\varepsilon_1(0)$. The estimated reflective index for α-B_{12}, $B_{11}C$-CBC and $B_{12}O_2$ are 2.60, 2.56 and 2.21 respectively. We are not aware of any measured data on stoichiometric single crystal samples or other calculations on the optical properties of these three crystals. There exist some reported optical absorption measurements but the data are difficult to interpret because of the presence of defect induced gap levels and lack of data at higher absorption energy.

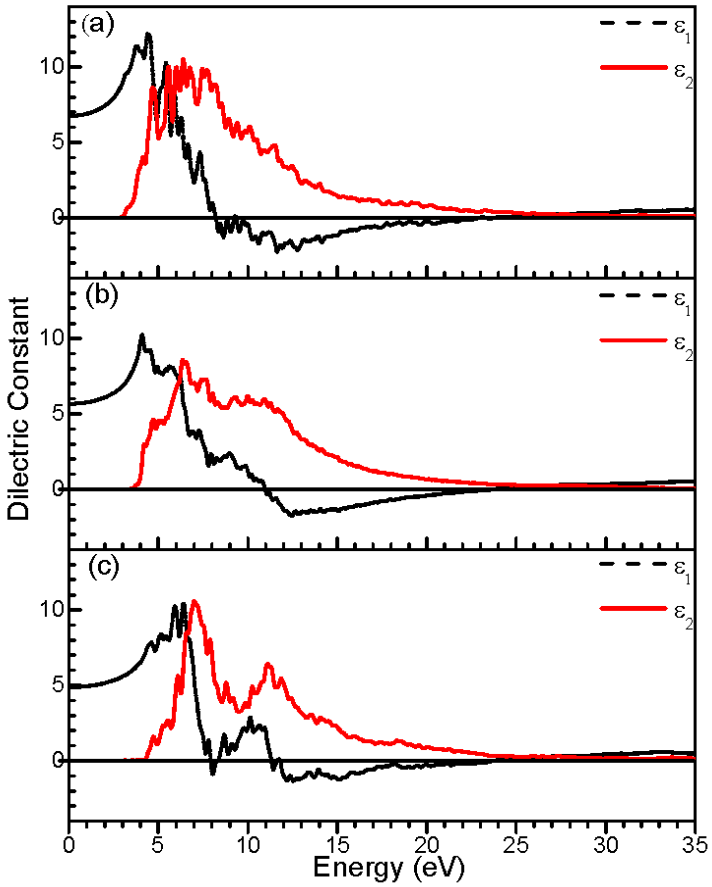

Figure 16. Dielectric function of three phases: (a) α-B_{12}; (b) B_4C and (c) $B_{12}O_2$

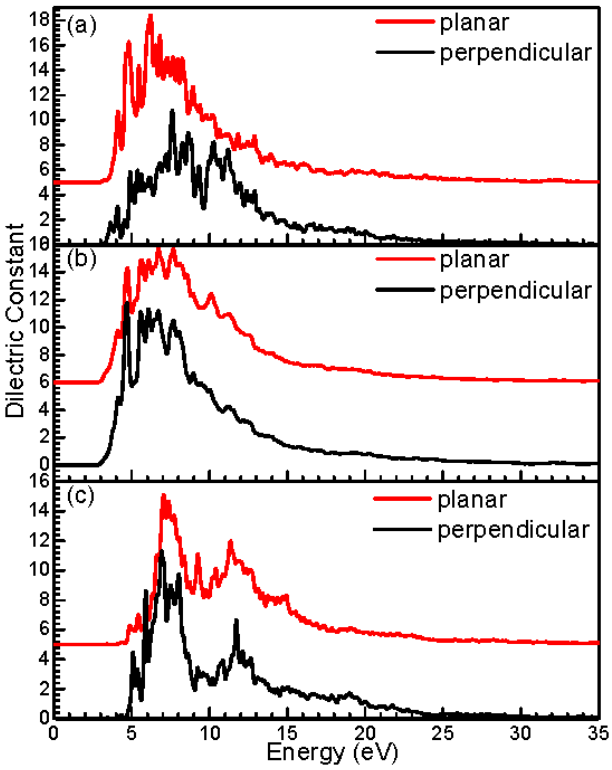

Figure 17. Direction resolved dielectric functions of the boron phases. (a) α-B_{12}; (b) B_4C and (c) $B_{12}O_2$

Vibration

Thermodynamic properties of a crystal which involve temperature, pressure and volume as fundamental variables start with its phonon spectrum. *Ab initio* calculations of vibrational and thermodynamic properties within the quasi-harmonic approximation (QSA) are computationally intensive especially for more complex crystals. For accurate evaluation of phonon spectrum, supercell must be used to give phonon dispersion $\omega_i(V,\vec{q})$ where V is the crystal volume and $\vec{q}$ is the phonon wave vector. We used a 2x2x2 supercell for the three crystals. A small displacement is applied to each atom in the crystal and the calculated force on each atom is used to construct the dynamic matrix. Its diagonalization gives the 3N modes (3 accuostic and 3N-3 optical) where N is the number atoms in the cell. We have neglected the correction for the longitudinal optical (LO) and transverse optic (TO) splitting since the LO-TO splitting is important mostly for ionic crystals.

Figure 18 shows the calculated phonon spectra and phonon DOS of a-B_{12}, B_4C and $B_{12}O_2$ crystals. As can be seen, these phonon dispersion and DOS are quite different from each other. In the low frequency region (< 500 cm^{-1}), B4C has more phonon modes than the other two crystals. All three crystals have the most enhanced peak in the DOS near 800 cm^{-1} and this can be attributed to the breathing modes of atoms within the icosahedral unit. It is also interesting to note that B4C has a single high frequency mode at 1622 cm^{-1} (not shown in Fig.2) which is absent in other two crystals. Obviously, this high frequency mode is related to the very short B-C bond within the CBC chain.

Raman and infra-red (IR) spectroscopy are popular experimental techniques to investigate the structure and mechanical properties in Boron and Born compounds. Our calculated zone center modes which include the Raman and IR active modes together with silent modes are

displayed in Figure 19. For α-B_{12}, all experimentally observed Raman modes can be identified in the calculated data (Fig. 19(a)) within an acceptable range of difference. The lowest four frequencies are at 500, 518, 577.9 and 607.8 cm^{-1}. The 518 cm^{-1} mode is close to the lowest experimental Raman frequency 527 cm^{-1} measured by Tallant et. al. and 525 cm^{-1} by Vast et. al which was attributed to be an icosahedral librational mode. Our highest frequency mode at 1188 cm^{-1} is almost the same as the measured one at 1186 cm^{-1}. The mode at 817.7 cm^{-1} appears to be coincide with the main peak in our phonon DOS.

Figure 19(b) shows the calculated zone center modes in B4C. The four lowest frequency modes are at 360, 398.9, 437.3 and 490.7 cm^{-1} which are in good agreement with the calculations of Lazzari et al with the exception of the lowest mde. All the Raman modes reported by Tallant et.al are present in our calculated modes. Two of these modes at 485 and 537.6 cm^{-1} are very close to the measured ones at 481 and 534 cm^{-1}. However, in the higher frequency region, the measured peaks are quite broadened so it is difficult to compare with individual calculated frequencies. The highest mode at 1622 cm^{-1} which is absent in α-B_{12} and $B_{12}O_2$ must have originated from the stretching modes within the CBC chain since they have short B-C bonds. This may be related to the infrared band at 1500 cm^{-1} reported by Jacobsohn et al on sputtered boron carbide film.

The calculated zone center frequency modes in $B_{12}O_2$ are displayed in the Figure 19 (c). The four lowest modes are at 427.2, 461.9, 527.6, and 552.6 cm^{-1} whereas the highest mode is at 1107.4 cm^{-1}. Measured Raman spectra by Wang et al and disagree with each other. Wang et al reported a high Raman active mode at 1181 cm^{-1} which disagrees with the Raman measurement Werheit et al nor in our calculation. Raman measurement shows one mode at an even higher

frequency 1243 cm^{-1} but was labeled it as uncertain whereas the second highest frequency at 1119 cm^{-1} is close to our calculated mode at 1107.4 cm^{-1}. Both Raman measurements have one lower frequency mode at 400 cm^{-1} (IR active) that is not reproduced in our calculation. Our calculation appears to be in favor of a Raman frequency at 773 cm^{-1} that was also marked as uncertain. On the other hand, our calculation strongly favors another uncertain mode at frequency 897cm^{-1}. All other measured Raman and IR frequencies can be identified in our calculation within an acceptable range of deviation. Very recently, Solozhenko et al reported the first order Raman spectrum of $B_{12}O_2$. Comparing their data with our calculated zone center vibrational modes of Figure 19 (c) the lower frequency modes (**< 600 cm-1**) are slightly lower than the calculated ones and the higher frequency modes (**> 1000 cm-1**) appear to be higher than the calculated ones, while the middle range frequencies are in good agreement. It is likely that the middle ranged frequencies are the vibrational modes from the B icosahedron whereas the lower and the high frequency models are more related to the O ions and the discrepancy is likely to be due to the O deficiency in the samples which certainly distort its frequencies. So, the situation in $B_{12}O_2$ crystal is rather confusing mainly due to the purity and nature of the samples measured. Further experimental and theoretical investigations are necessary.

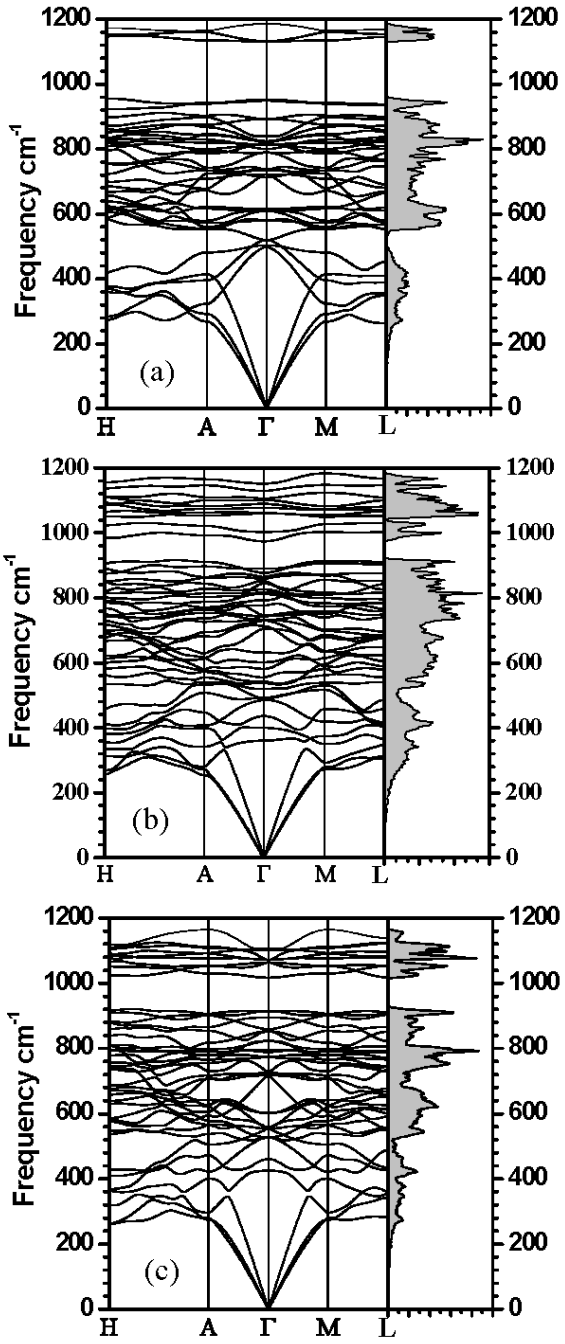

Figure 18. Phonon dispersion and density of states of the boron phases. (a) α-B_{12}; (b) B_4C and (c) $B_{12}O_2$

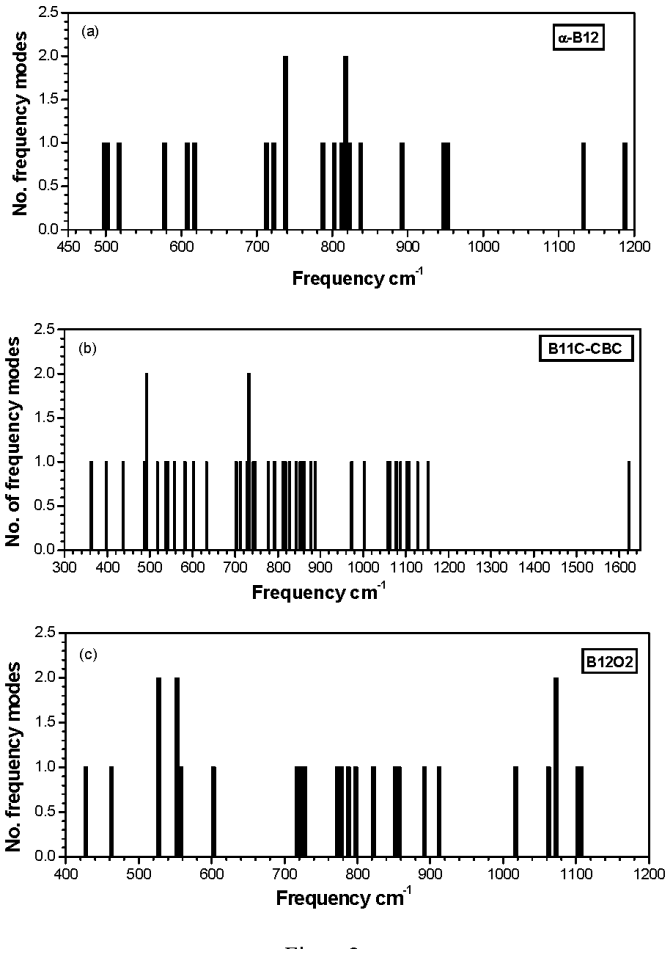

Figure 19. Phone frequencies of three boron phases. (a) α-B_{12}; (b) B_4C and (c) $B_{12}O_2$

Thermodynamical Properties

The study of thermodynamic properties of these crystals follows the calculated phonon spectra. From the phonon spectra, we can obtained Holmholtz free energy F(V,T). The Gibbs free energy *G(P,T)* and enthalpy *H(P,T)* can be evaluated according to general thermodynamic relations

$$G(P,T) = F(V,T) + PV; \qquad H(P,T) = G(P,T) + TS \tag{7}$$

where *S* is the vibrational entropy given by:

$$S^{vib}(V,T) = \sum_{\vec{q}}^{BZ}\sum_{i}^{3N}\{k_B \ln(1-e^{-\hbar\omega_i(V,\vec{q})/k_BT}) + \frac{\hbar\omega_i(V,\vec{q})}{T}\frac{e^{-\hbar\omega_i(V,\vec{q})/k_BT}}{1-e^{-\hbar\omega_i(V,\vec{q})/k_BT}}\} \tag{8}$$

In the actual calculation of *G(P,T)*, we first obtain *F(V,T)* of the crystal at seven different volumes by scaling the lattice constants of the equilibrium structure by -3% to 3% in 1% increments. This entails the calculation of the phonon spectra at seven different volumes. The seven data points for the free energy are fitted to a fourth order polynomial and pressure P at a given volume V is obtained by direct differentiation $P(V,T) = -(\partial F/\partial V)_T$.

The calculated Gibbs' free energies *G(P,T)* for the three crystals are presented in Figure 20 in the form of colored contour plots. Since these three crystals have different number of atoms per unit cell, a direct comparison would be difficult so the results for the Gibbs free energy are expressed in the unit of energy per atom. As can be seen, a-B_{12} has much higher G(P,T) at high temperature and pressure. B_4C has relatively smaller G(P,T) per atom followed by $B_{12}O_2$ indicating that these two crystals should have higher stability at high pressures and high temperatures. In particular, B_4C has a much lower Gibbs free energy at high temperature and

low pressure consistent with many experimental observations related to its applications. However, we should also be aware that these calculations are based on QHA which would be less valid for temperatures above 1600K. The more distinguished thermodynamic properties of B_4C and $B_{12}O_2$ obviously related to the presence of additional atoms or chain of atoms. It would be interesting to use the present technique to calculate G(P,T) for possible thermodynamic phases transitions to between crystals of same composition, for example between a-B12 and β-boron or γ-boron. Masago and co-workers have studied the crystal stability and thermodynamic properties of a-B12 and beta-B105 and concluded that a-B12 is more stable than b-B_{105}. Shang et el had also calculated the phonon spectra and the Helmholtz free energy F of a-B_{12} and b-B_{105} with a conclusion that a-B_{12} is thermodynamically more stable than b-B_{105} below 1388K. However, these calculations are for a fixed volume with temperature as the only variable the fact that the exact structure of beta boron is defective and unknown. It would be desirable to extend the present *G(P,T)* calculation to a realistic models of b-boron.

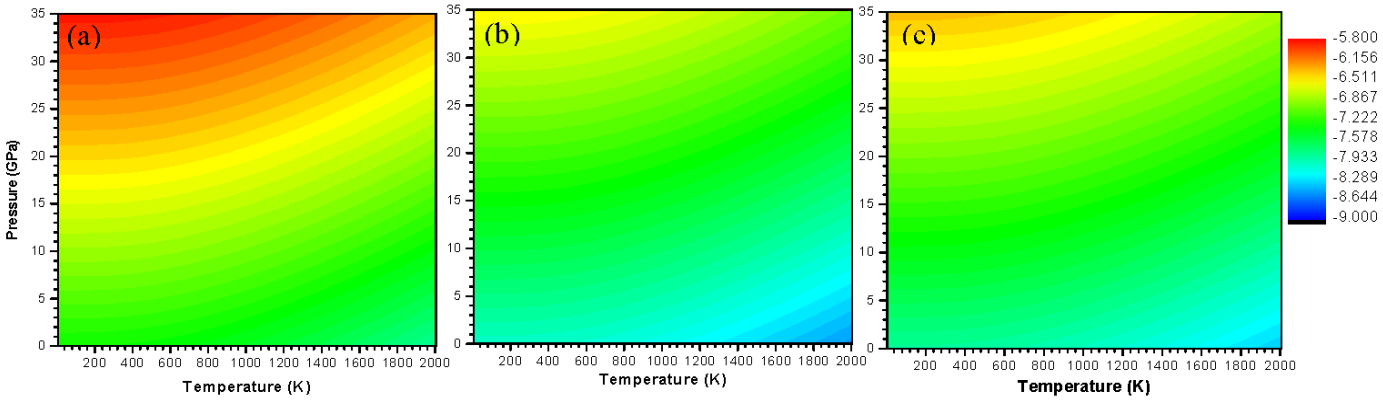

Figure 20. Gibbs free energy contour plots of the three boron phases: (a) α-B_{12}; (b) B_4C and (c) $B_{12}O_2$

XANES

XANES/ELNES spectroscopy is powerful characterization technique to obtain information about the electron states of the unoccupied CB states related to the bonding environment of a particular atom in a solid. Experimentally, it is generally difficult to obtain the XANES/ELNES spectrum of a specific edge at a particular site and the measured spectrum is the averaged spectrum over different sites of the same type of atoms. One of the main developments of the OLCAO method in recent years is the *ab initio* calculation s of the XANES or ELNES spectrum of a crystal using a supercell approach. The supercell-OLCAO method can provide the theoretical spectrum at any atomic site thereby facilitating the interpretation of measured spectra. In complex crystals with many different nonequivalent sites of different local geometry such as in B and B compounds, such calculations are very valuable. Here we present the XANES/ELNES spectra of all non-equivalent atomic sites and their weighted sums which are then compared with the measured spectra. The steps of the calculation in the supercell-OLCAO method have been described in great detail in a recent paper and will be repeated here. This method has been successfully applied to obtain the XANES/ELNES spectra of many crystals and their defects. XANES/ELNES spectroscopy have been extensively used to characterize the structure and composition of B and B compounds.

The B-K edge for α-B_{12} [Figure.21] has been presented in a brief paper in conjunction with the calculation on γ-B_{28} phase. The total spectrum (top panel) is the weighted sum of the spectra of B_{polar} and B_{equat} in equal proportions. They are quite different because of their different bonding environments. B_{polar}-K has more peak features than B_{equat}-K. Furthermore, the edge onset of B_{polar}-K is shifted towards lower energy. In Figure 22, we use the same labels for the peaks in the individual spectra as in the total spectrum so as to show which one contributes to which. The shoulder peak A at the edge (192.9 eV) comes from B_{polar}-K. Peak B (194.2 eV) has

contributions from both B_{polar}-K and B_{equat}-K whereas peak C (195.4 eV) is unquestionably from B_{equat}-K. At intermediate energies, Peaks D and E are less prominent because of partial cancelations from the contributions from two sites. Peak F (201.0 eV) is mostly from B_{polar}-K and G (202.4 eV) is mostly from B_{equat}-K. At the higher energy range, peaks H, I, J are identified in the total spectrum and the relatively prominent peak J is exclusively from B_{polar}-K. In Figure 23 we compare the calculated XANES/ELNES spectrum of α-B12 with corresponding experimental spectrum. Our calculation has reproduced all peak features present in the experiment spectrum. This is achieved only if we take the total spectrum to be the weighted sum of different spectra from individual nonequivalent sites.

The calculated B-K and C-K edges for B4C are shown in Figure 24 and Figure 25 respectively. As in α-B12 case spectra for individual sites have very different features especially for the B atom in the middle of the three atom chain. The peak A (196.0 eV) in the total spectrum is also the most pronounced peak and is the combined contribution from three B sites. The minor peaks B (198.2 eV) and E are both from the B_{equat}-K. Another prominent peak C (201.1 eV) is almost equally contributed by B_{polar}-K and B_{equat}-K. Similarly, peak F (207.5 eV) is shaped by both B_{polar} and B_{equat}. Peak H (215.3 eV) at a higher energy is exclusively from the B atom in the C-B-C chain. We can also identify some minor peaks D and G which have contributions from both B_{polar} and B_{equat}. The K-edge spectrum of chain boron has only two peaks, A" and H. A" contributed to the broadening of A in the total spectrum and H is the well pronounced peak H at higher energy. These spectroscopic features are radically different from those of B_{polar} and B_{equat} because of entirely different local geometry. The K-edges for the polar and chain C atoms shown in Figure 25 (a) also have very different features because of the different local bonding configurations. As a matter of fact, the C_{polar}-K resembles more the B_{polar}-K than the chain C-K

edge spectrum! The total C-K spectrum has a main peak D (294.2 eV) which is almost equally contributed from both C sites. There are some less prominent shoulder-like peaks on both sides of peak D. As can be clearly seen, the edge peak A (289.7 eV) is from the chain C whereas the sharp peak B (291.8 eV) is from polar C. The well produced peak G (309.3 eV) and H (321.0 eV) at the higher energy is exclusively from that of chain C-K. In Figure 26, we compare the calculated B-K and C-K with the corresponding experimental spectrum in B_4C . The edge peak A which is also the most pronounced peaks is aligned up by shifting the calculated spectrum by 4.47 eV. The agreement is very satisfactory. The calculated spectrum has reproduced all peak features present in the experiment. In case of C-K edge in B4C it is clearly shown that the calculated spectrum as the sum of two different C sites has a much richer spectrum than the measured data which is also limited by the experimental resolution. But the general shape is in good agreement except the position of the leading peak. The calculated total B-K and C-K edges in B4C are also in good agreement with the XANES spectra obtained by Jimenz et al on polycrystalline samples before heating and the very similar B-K edge measured by Li et al. In these comparisons, we have to contend that some of the disagreement could be root from the different samples of the boron carbide and the limited instrumental resolution available at the time of measurements.

The calculate B-K edge spectra of B12O2 are shown in Figure 27. Interestingly, B_{polar} and B_{equat} have rather similar peak features but with different edge onset. This shift in energy onset between polar and equatorial sites resulted in more peak features in the total B-K spectrum. The prominent peak A (196.5 eV) at the edge onset and other two peaks D (201.5 eV) and F (207.6 eV) in total are from the related peaks in B_{polar}-K spectrum whereas the main peak B (198.2 eV), peak E (203.0 eV) and peak G (209.6 eV) are from B_{equat}-K spectrum.

In Figure 28, we compare the calculated B-K and O-K spectra in B12O2 with corresponding experimental spectrum. As we can be seen, all the peak features in B-K edge present in the measured spectrum are reproduced by the calculation. Not only peak positions but also the overall shape of the spectrum is in good agreement. For the O-K edge, the calculated spectrum has a strong peak A and other well-resolved peaks at higher energy. Peak A is in good agreement with experiment, peak B is at a slightly higher energy whereas peak C in the calculated spectrum is somewhat less prominent but its relative position with B still matches with the experiment. The overall agreement seems satisfactory since the general spectral shape is similar even in the high energy range where the experimental resolution is limited. Some of the discrepancies may also be attributed to the fact that the samples used in the experiment are not stoichiometic of $B_{12}O_2$ and may be O-deficient.

To assess the overall features of the B-K edges in α-B_{12}, B_4C and $B_{12}O_2$ crystals, we compare their total B-K spectra in Figure 29. Obviously, they are very different in peak features as well as on energy onsets. The energy onset of B-K edge in α-B_{12} is significantly lower than that of the other two. The edge onset of B-K in B_4C is slightly lower than that of $B_{12}O_2$. B-K edge in α-B_{12} has more peak features and more broadened overall spectral shape than in other two crystals in spite of the fact that a-B12 is an elemental B without any other elements. The fact that such complicated spectra can reproduce all the experimentally observed features well is truly amazing and bears a strong testimony to the theory and techniques used in the supercell-OLCAO method for XANES/ELNES calculations. In ref. 50 where the XANES/ELENES spectrum of γ-B28 was compared with that of a-B_{12}, it was pointed out that there were resemblances in the spectral features of B-K edges of B_{polar} and B_{equat} with similar sites in γ-B_{28} in the icosahedral

unit. Such similarities no longer exist in the present case with B_4C and $B_{12}O_2$. This underscores the importance of the presence of the chain atoms or O atoms in the crystal in modifying the spectral features of B-K edge.

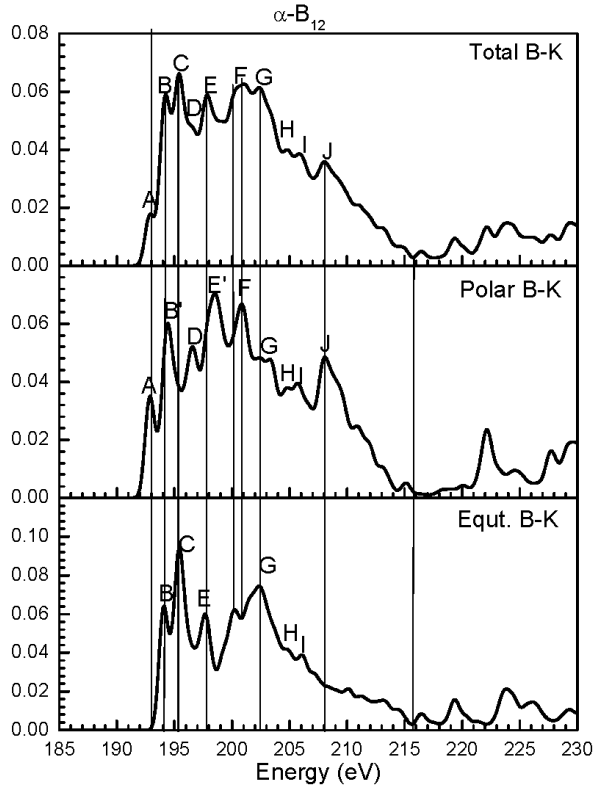

Figure 21. Calculated B-K edge in α-B_{12}. Top panel is total weighted sum of individual spectr.

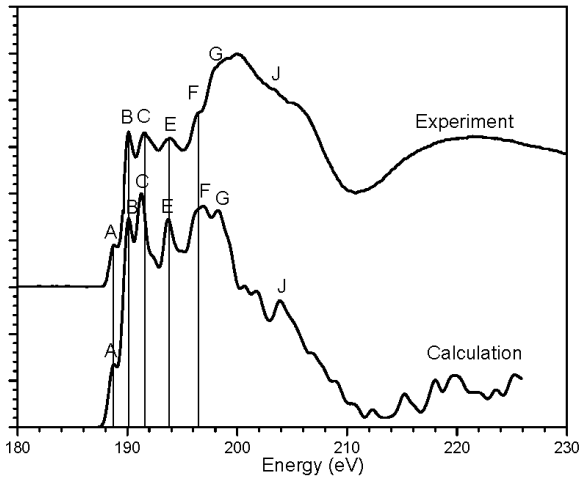

Figure 22. Comparison between calculated and measured B K edge in a-B_{12}. The theoretical spectrum is shifted by 4.09 eV to align the main peak with experiment.

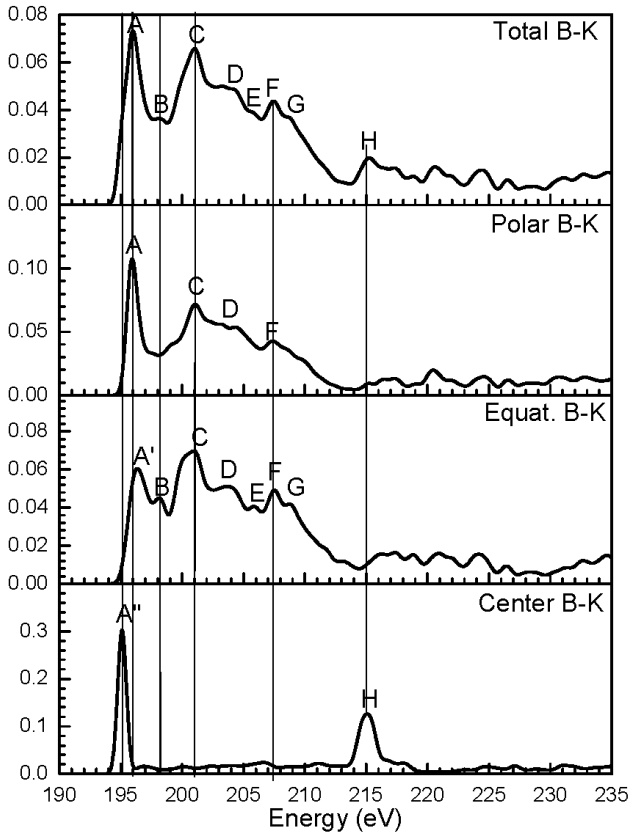

Figure 23. Calculated B-K edge in B_4C. Top panel is the weighted sum of the spectra from different sites (lower panels).

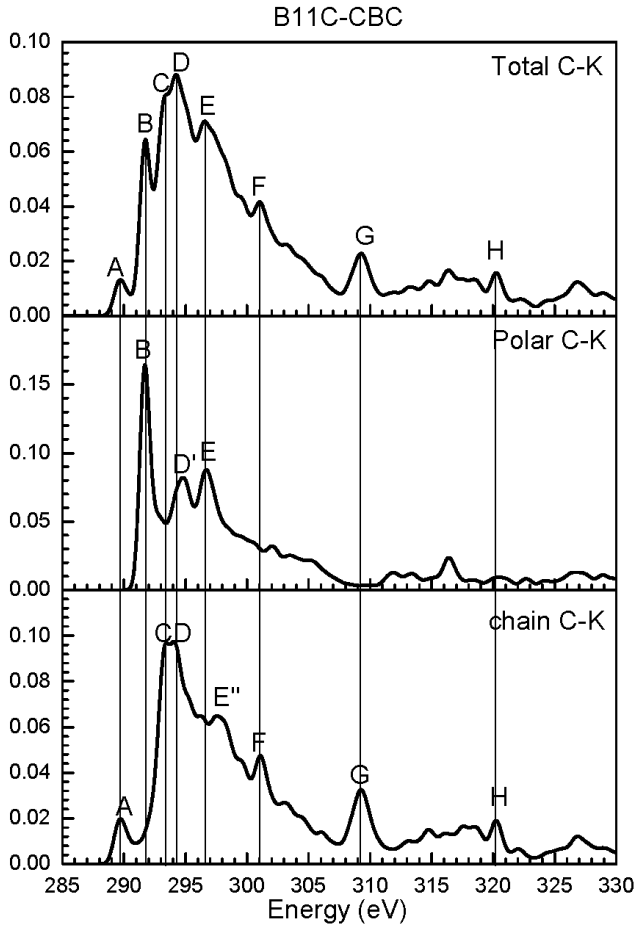

Figure 24. C-K edge in B4C: Top panel is the weighted sum and the lower panels are spectra for C in the chain and in the polar site of the icosahedrons.

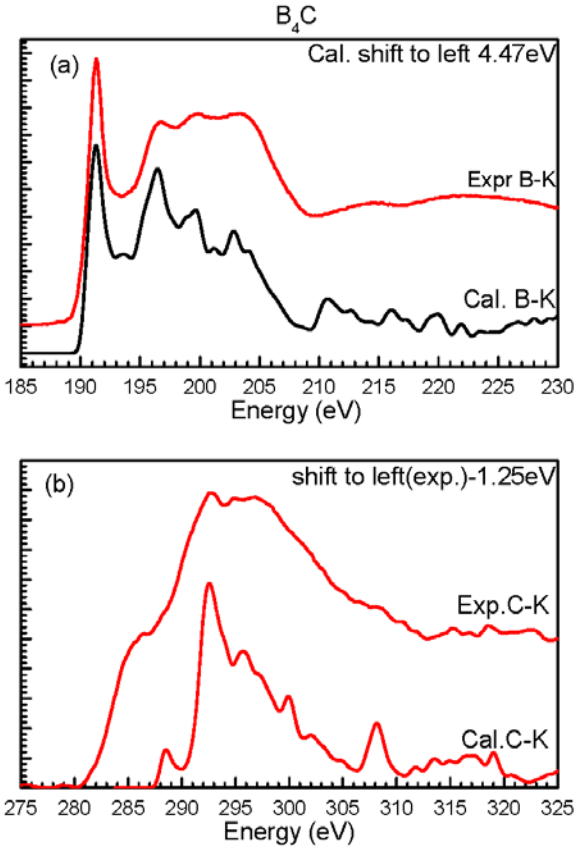

Figure 25. Comparison between the calculated and the measured ELNES spectra in B4C: (a) B-K; (b) C-K. The calculated spectrum is shifted by 4.47 eV to align the main peak with experiments .

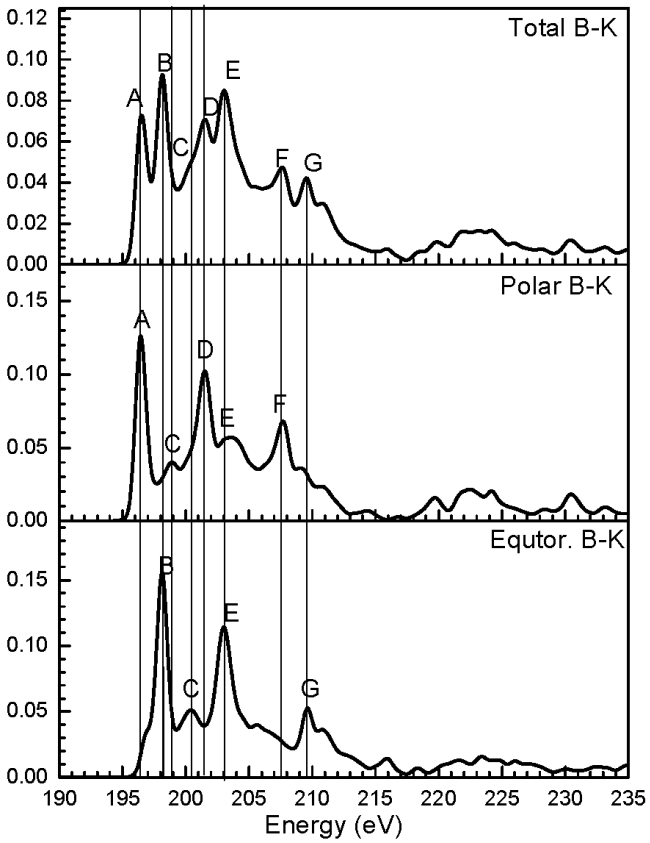

Figure 26. Calculated B-K edge in B12O2. Top panel is the weighted sum and the lower panels are the spectra from polar and equatorial B sites.

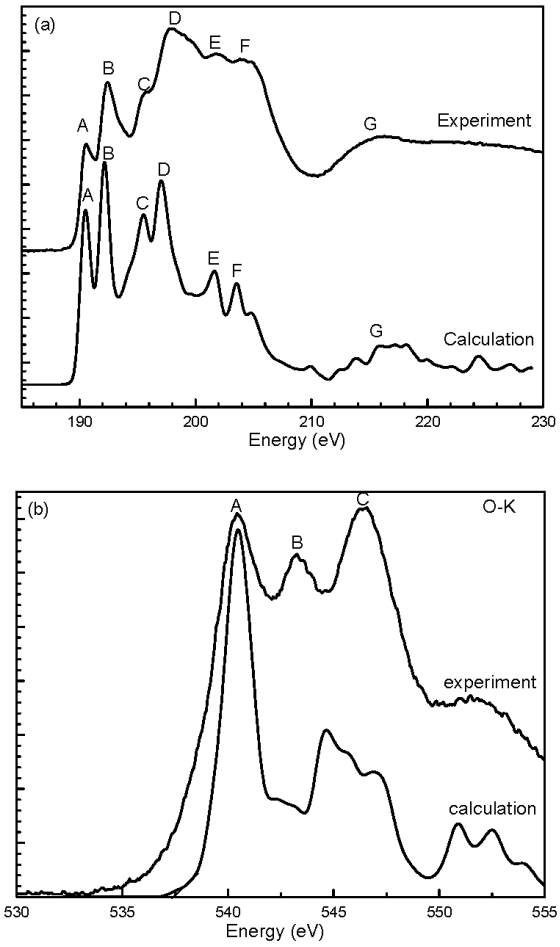

Figure 27. Comparison of the calculated (total) and the measured B-K edge (a), and O-K edge (b). The calculated spectrum is shifted by 3.94 eV for B-K and 5.69 eV for O-K to align the main peaks with experiment.

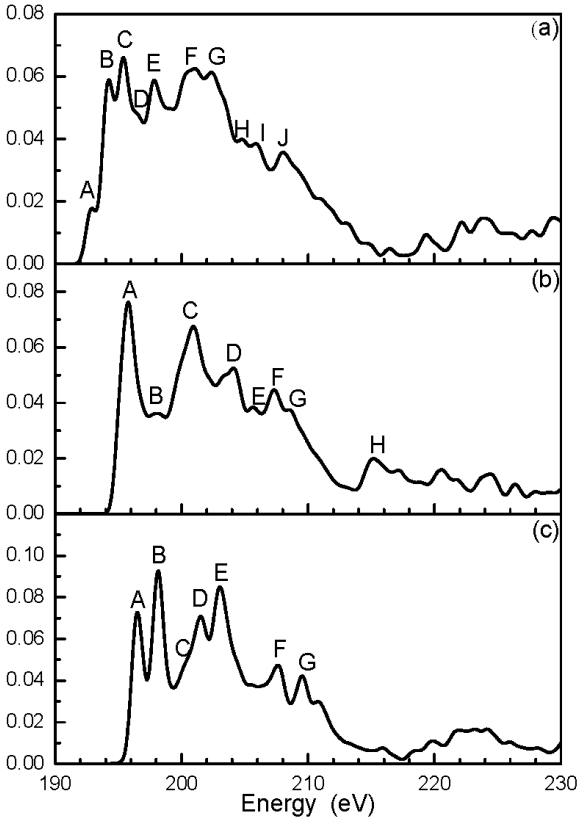

Figure 28. Comparison of the calculated B-K spectra (total) of (a) α-B_{12}; (b) B_4C and (c) $B_{12}O_2$.

V. CONCLUSIONS

In summary, we have developed software tools for study complex crystals with partial occupations and applied them to boron carbides.

Two methods have been implemented in our first principles methods based G(P,T) package: (1) supercell sampling method; (2) unitcell expansion method. In addition, we have developed the pressure dependent elastic constant module.

Carbon distribution in boron carbide is central to understand its structure-properties relation. Determination of carbon distribution from experiments has so far been inconclusive due to various technical issues. We used both the supercell method and the unitcell expansion method to study the carbon distribution. Our results suggest that depending on the carbon concentration, starting from lower end:

- The carbon first filled the end sites of the 3-atom chains in boron,
- Additional carbon will take the equatorial sites in the B_{12} icosahedrons with a small percentage will go to the central site of the 3-atom chains.
- At higher carbon concentration, $[B_{10}C_2]$C-B-C type of structure started to emerge.

We further studied the mechanical behavior of boron carbide under uniaxial load. Boron carbide suffers from dramatic decrease of shear strength when impact goes beyond the Hugonoit Elastic Limit (HEL) of about 22GPa. Post-failure analysis attributes the loss of shear strength to local amorphization. We performed uniaxial compression simulation of boron carbide using a supercell model. We observed, however, amorphization of boron carbide at much higher stress of about 160GPa.

For selected models, we computed the vibrational properties and X-ray absorption near edge structure. We also searched extensively high symmetry supercell models and did not find any low energy configuration that warrants further studies.

VI. FACILITIES AND RESOURCES

We have built an 18-node cluster using AMD phenom™ 6-core CPU. Among them, 16 nodes are dedicated to computing, 1 node serves as head node that provides internet interface and cluster management, and 1 node is dedicated to storage service. Each computing node has 4GB memory. 8 nodes have 1TB hard drive and the other 8 nodes are equipped with 60GB solid state disk. A 8TB storage array is used to provide the shared cluster file system for scratching.

REFERENCES,

1. D. Gosset and M. Colin, *Boron carbides of various compositions. An improved method for x-rays characterisation*, Journal of Nuclear Materials **183** (1991), no. 3, 161-173.
2. F. Thevenot, *Boron carbide - a comprehensive review*, Journal of the European Ceramics Society **6** (1990), no. 4, 205-225.
3. H. Werheit, *Boron-rich solids - a chance for high-efficiency high-temperature thermoelectric energy-conversion*, Materials Science and Engineering B-Solid State Materials for Advanced Technology **29** (1995), no. 1-3, 228-232.
4. S. D. Hwang, D. Byun, N. J. Ianno, P. A. Dowben and H. R. Kim, *Fabrication of boron-carbide/boron heterojunction devices*, Applied Physics Letters **68** (1996), no. 11, 1495-1497.
5. M. Calandra, N. Vast and F. Mauri, *Superconductivity from doping boron icosahedra*, Physical Review B **69** (2004), no. 22.
6. T. L. Aselage, D. Emin and S. S. McCready, *Conductivities and seebeck coefficients of boron carbides: Softening bipolaron hopping*, Physical Review B **6405** (2001), no. 5, -.
7. U. Kuhlmann and H. Werheit, *On the microstructure of boron-carbide*, Solid State Communications **83** (1992), no. 11, 849-852.
8. G. H. Kwei and B. Morosin, *Structures of the boron-rich boron carbides from neutron powder diffraction: Implications for the nature of the inter-icosahedral chains*, Journal of Physical Chemistry **100** (1996), no. 19, 8031-8039.
9. R. Lazzari, N. Vast, J. M. Besson, S. Baroni and A. Dal Corso, *Atomic structure and vibrational properties of icosahedral b4c boron carbide*, Physical Review Letters **83** (1999), no. 16, 3230-3233.
10. F. Mauri, N. Vast and C. J. Pickard, *Atomic structure of icosahedral b4c boron carbide from a first principles analysis of nmr spectra*, Physical Review Letters **8708** (2001), no. 8, -.
11. K. Shirai and S. Emura, *Lattice vibrations and the bonding nature of boron carbide*, Journal of Physics-Condensed Matter **8** (1996), no. 50, 10919-10929.
12. ---, *Lattice vibrations of boron carbide*, Journal of Solid State Chemistry **133** (1997), no. 1, 93-96.
13. N. Vast, J. M. Besson, S. Baroni and A. Dal Corso, *Atomic structure and vibrational properties of icosahedral alpha-boron and b4c boron carbide*, Computational Materials Science **17** (2000), no. 2-4, 127-132.
14. D. M. Bylander and L. Kleinman, *Structure of b13c2*, Physical Review B **43** (1991), no. 2, 1487-1491.
15. G. Fanchini, J. W. McCauley and M. Chhowalla, *Behavior of disordered boron carbide under stress*, Physical Review Letters **97** (2006), no. 3, -.
16. A. Kirfel, A. Gupta and G. Will, *The nature of the chemical bonding in boron carbide, b13c2. I. Structure refinement*, Acta Crystallographica Section B **35** (1979), no. 5, 1052-1059.
17. K. F. Cai, C. W. Nan, M. Schmuecker and E. Mueller, *Microstructure of hot-pressed b4c-tib2 thermoelectric composites*, Journal of Alloys and Compounds **350** (2003), no. 1-2, 313-318.
18. S. Lee, D. M. Bylander and L. Kleinman, *Elastic moduli of b12 and its compounds*, Physical Review B **45** (1992), no. 7, 3245.
19. R. J. Nelmes, J. S. Loveday, R. M. Wilson, W. G. Marshall, J. M. Besson, S. Klotz, G. Hamel, T. L. Aselage and S. Hull, *Observation of inverted-molecular compression in boron-carbide*, Physical Review Letters **74** (1995), no. 12, 2268-2271.
20. T. L. Aselage, D. R. Tallant and D. Emin, *Isotope dependencies of raman spectra of b12as2, b12p2, b12o2, and b12+xc3-x: Bonding of intericosahedral chains*, Physical Review B **56** (1997), no. 6, 3122-3129.
21. O. Chauvet, D. Emin, L. Forro, T. L. Aselage and L. Zuppiroli, *Spin susceptibility of boron carbides: Dissociation of singlet small bipolarons*, Physical Review B **53** (1996), no. 21, 14450.

22. T. L. Aselage, D. Emin, S. S. McCready and R. V. Duncan, *Large enhancement of boron carbides' seebeck coefficients through vibrational softening*, Physical Review Letters **81** (1998), no. 11, 2316.
23. C. Wood, D. Emin and P. E. Gray, *Thermal conductivity behavior of boron carbides*, Physical Review B **31** (1985), no. 10, 6811.
24. M. M. Balakrishnarajan, P. D. Pancharatna and R. Hoffmann, *Structure and bonding in boron carbide: The invincibility of imperfections*, New Journal of Chemistry **31** (2007), no. 4, 473-485.
25. J. M. Sanchez, F. Ducastelle and D. Gratias, *Generalized cluster description of multicomponent systems*, Physica A: Statistical and Theoretical Physics **128** (1984), no. 1-2, 334-350.
26. L. Ouyang and W. Y. Ching, *Electronic structure and dielectric properties of dielectric gate material (zro[sub 2])[sub x](sio[sub 2])[sub 1 - x]*, Journal of Applied Physics **95** (2004), no. 12, 7918-7924.
27. L. Ouyang and W.-Y. Ching, *Prediction of a high-density phase of sio_{2} with a high dielectric constant*, physica status solidi (b) **242** (2005), no. 7, R64-R66.
28. L. Ouyang, S. Aryal, P. Rulis and W. Y. Ching, *To be published*, (2008).
29. G. Kresse and J. Furthm 黣 ler, *Efficiency of ab-initio total energy calculations for metals and semiconductors using a plane-wave basis set*, Computational Materials Science **6** (1996), no. 1, 15-50.
30. ---, *Efficient iterative schemes for ab initio total-energy calculations using a plane-wave basis set*, Physical Review B **54** (1996), no. 16, 11169.
31. G. Kresse and J. Hafner, *Ab initio molecular dynamics for liquid metals*, Physical Review B **47** (1993), no. 1, 558.
32. H. Yao, L. Ouyang and W.-Y. Ching, *Ab initio calculation of elastic constants of ceramic crystals*, Journal of the American Ceramic Society **90** (2007), no. 10, 3194-3204.
33. W. Y. Ching and C. C. Lin, *Orthogonalized linear combinations of atomic orbitals: Application to the calculation of energy bands of si iii*, Physical Review B **12** (1975), no. 12, 5536.
34. W. Y. Ching, *Theoretical studies of the electronic properties of ceramic materials*, Journal of the American Ceramic Society **73** (1990), no. 11, 3135-3160.
35. S.-D. Mo and W. Y. Ching, *Ab initio calculation of the core-hole effect in the electron energy-loss near-edge structure*, Physical Review B **62** (2000), no. 12, 7901.
36. W. Y. Ching and C. C. Lin, *Optical dielectric function of intrinsic amorphous silicon*, Physical Review B **18** (1978), no. 12, 6829.
37. W. Y. Ching, *Microscopic calculation of localized electron states in an intrinsic glass*, Physical Review Letters **46** (1981), no. 9, 607.
38. L. Ouyang, P. Rulis, W.-Y. Ching, M. Slouf, G. Nardin and L. Randaccio, *Electronic structure and bonding in hydroxocobalamin*, Spectrochimica Acta Part A: Molecular and Biomolecular Spectroscopy **61** (2005), no. 7, 1647-1652.
39. J. B. MacNaughton, A. Moewes, J. S. Lee, S. D. Wettig, H. B. Kraatz, L. Z. Ouyang, W. Y. Ching and E. Z. Kurmaev, *Dependence of DNA electronic structure on environmental and structural variations*, J. Phys. Chem. B **110** (2006), no. 32, 15742-15748.
40. J. Chen, L. Ouyang, P. Rulis, A. Misra and W. Y. Ching, *Complex nonlinear deformation of nanometer intergranular glassy films in beta-si[sub 3]n[sub 4]*, Physical Review Letters **95** (2005), no. 25, 256103-256104.
41. W. Y. Ching, L. Ouyang, H. Yao and Y. N. Xu, *Electronic structure and bonding in the y-si-o-n quaternary crystals*, Physical Review B **70** (2004), no. 8, 085105.
42. W.-Y. Ching, S.-D. Mo and Y. Chen, *Calculation of xanes/elnes spectra of all edges in si3n4 and si2n2o*, Journal of the American Ceramic Society **85** (2002), no. 1, 11-15.
43. I. Tanaka, T. Mizoguchi, M. Matsui, S. Yoshioka, H. Adachi, T. Yamamoto, T. Okajima, M. Umesaki, W. Y. Ching, Y. Inoue, M. Mizuno, H. Araki and Y. Shirai, *Identification of ultradilute dopants in ceramics*, Nat Mater **2** (2003), no. 8, 541-545.

44. R. Hill, *The elastic behaviour of a crystalline aggregate*, Proceedings of the Physical Society. Section A **65** (1952), no. 5, 349-354.
45. P. D. Tepesch, A. F. Kohan, G. D. Garbulsky, G. Ceder, C. Coley, H. T. Stokes, L. L. Boyer, M. J. Mehl, B. P. Burton, K. Cho and J. Joannopoulos, *A model to compute phase diagrams in oxides with empirical or first-principles energy methods and application to the solubility limits in the cao-mgo system*, Journal of the American Ceramic Society **79** (1996), no. 8, 2033-2040.
46. V. S. Urusov, *Comparison of semi-empirical and ab initio calculations of the mixing properties of mo-m ' o solid solutions*, Journal of Solid State Chemistry **153** (2000), no. 2, 357-364.
47. M. Konigstein and C. R. A. Catlow, *Ab initio quantum mechanical study of the structure and stability of the alkaline earth metal oxides and peroxides*, Journal of Solid State Chemistry **140** (1998), no. 1, 103-115.
48. J. L. Hoard and R. E. Hughes, *The chemistry of boron and its compounds*, Wiley, New York, 1967, p. 25.

49 S. Lee, et al, Phys. Rev. B, 44, 3550 (1991). Electronic structure B6O; S. Lee, et al, Phys. Rev. B, 42, 1316 (1990). Electronic structure a-B-12; D.M. Bylander, et al, Phys. Rev. B, 42, 1394 (1990); D.M. Bylander, et al, Phys. Rev. B, 45,3245 (1992).
50 Paul Rulis, Liaoyuan Wang and W.Y, Ching, "Prediction of the XANES/ELNES spectra of γ-B28 and comparison with α-B12", Phys. Status Solidi RRL 3, 133-135 (2009).